INTERNATIONAL JOURNAL FOR NUMERICAL METHODS IN FLUIDS, VOL. 10, 79–117 (1990)

BUOYANCY-DRIVEN INSTABILITY IN A VERTICAL CYLINDER: BINARY FLUIDS WITH SORET EFFECT. PART I: GENERAL THEORY AND STATIONARY STABILITY RESULTS

G. R. HARDIN AND R. L. SANI

Department of Chemical Engineering, Center for Low-Gravity Fluid Mechanics and Transport, University of Colorado, Boulder, CO 80309-0432, U.S.A.

D. HENRY

Département de Physique des Matériaux, Université Claude Bernard, F-69622 Villeurbanne Cedex, France

AND

B. ROUX

Institut de Mécanique des Fluides, 1 Rue Honnorat, F-13003 Marseille, France

SUMMARY

Buoyancy-driven instability of a monocomponent or binary fluid which is completely contained in a vertical circular cylinder is investigated, including the influence of the Soret effect for the binary mixture. The Boussinesq approximation is used, and the resulting linear stability problem is solved using Galerkin's technique. The analysis considers various types of fluid mixtures, ranging from gases to liquid metals, in cylinders with a variety of radius-to-height ratios. The flow structure is found to depend strongly on both the cylinder aspect ratio and the magnitude of the Soret effect. Comparisons are made with experiments and other theories, and the predicted stability limits are shown to agree closely with observations.

KEY WORDS Fluid mechanics Stability Soret effect Buoyancy-driven Double diffusive

1. INTRODUCTION

Buoyancy-driven instability of a quiescent, horizontal monocomponent layer of fluid heated from below in the presence of a gravitational field has been the subject of many previous investigations. These experimental and theoretical studies encompass both layers of infinite as well as finite lateral extent, although studies of the former are much more numerous. It is well known that when the imposed temperature gradient leads to a sufficiently large unstable density gradient, characterized by a certain critical value of the Rayleigh number, flow and structure ensue. The original variants of the problem with thermally induced density stratification have since been complemented by the inclusion of double-diffusive effects, so that concentration as well as temperature fields can play a major role. The latter demonstrated the occurrence of an instability whose mechanism relied on the differences in relaxation times between the temperature and concentration fields.[1-3] In such multifield systems there is also the possibility of additional

0271–2091/90/010079–39$19.50

Received 21 March 1988
Revised 20 April 1989

coupling through the Soret and Dufour effects, alias thermal diffusion effect and the diffusion-thermo effect respectively.[4] One focus of the present study is the effect of such coupling on the stability of a vertical, bounded cylindrical layer of a binary mixture. The stability of such systems can be adversely affected by the Soret effect, i.e. mass transfer driven by a temperature gradient, if the heavier species tends to move towards the cold region, producing an adverse contribution to the density gradient when heating is from below. In some cases a substantial decrease in the stability of the system is realized.

Despite the potential importance of the Soret effect in certain systems, both the Soret and Dufour effects were ignored compared to ordinary diffusion and conduction respectively until the importance of *double-diffusive* effects was recognized. Then, both experimental (e.g. References 5–12) and theoretical (e.g. References 13–16) studies established the importance of the Soret effect in many systems, either as a primary mechanism leading to instability and subsequent flow, or as the mechanism which generates a precursor disturbance to trigger a flow in which it plays a minor role.[17] Recent interest in the Soret effect has also been stimulated by the growing possibility of conducting materials science experiments and physical property measurements in a low-gravity environment, i.e. crystal growth from solution or vapour phase deposition on Skylab[18] or space shuttle missions, or accurate measurements of Soret coefficients.[19] In exploring the latter, Bataille *et al.*[20] conducted a linear stability analysis of a horizontally infinite binary fluid layer subjected to a temperature gradient. Their analysis included the possibility of the Soret effect and also surface tension driving forces, which could be important in the low-gravity environment. Castillo and Velarde[21] performed a similar analysis in which the case of overstability was also considered. Villers and Platten[22] reported some interesting experimental observations of instability in an isopropal alcohol and water mixture (9·1 wt.% alcohol), which exhibits a noticeable Soret effect. More comprehensive reviews are presented by Schechter *et al.*[23] and Platten and Chavepeyer.[24]

More recently, the importance of the Dufour effect has become a topic of interest. Ybarra and Velarde[25] and Gutkowicz-Krusin *et al.*[26,27] have suggested that the Dufour effect could play an important role in determining the stability of a binary gas mixture, since for gases $\kappa/D \approx 1$, so that the Soret and Dufour effects act on comparable time scales. (Here κ and D are the thermal and mass diffusivities respectively.) Ybarra and Velarde studied the linear, steady, horizontally infinite fluid layer problem for a binary mixture with Soret and Dufour effects and stress-free top boundary conditions. Gutkowicz-Krusin *et al.* studied a similar system with either stress-free or no-slip top boundary conditions, but considered both steady and oscillatory convection and a broader range of parameters than in the preceding work. However, as pointed out by Abernathey and Rosenberger,[28] the latter study appears to have confused the mass and mole average thermal diffusion ratio, which could lead to misinterpretation of their results.

Recently, the influence of the lateral size of the system on its stability has been investigated theoretically for a domain of cylindrical cross-section.[29–33] These analyses were stimulated by the detailed observations of Abernathey and Rosenberger,[28] who conducted a series of experiments to determine the critical Rayleigh number for the onset of convection of a binary mixture heated from below in a narrow vertical cylinder with highly conducting walls. These experiments considered a variety of bulk concentrations of xenon–helium (Xe–He) and xenon–argon (Xe–Ar) mixtures. They found that the sidewall substantially affected the stability of these mixtures. The lateral wall was observed to be convectively less stabilizing for the binary systems which they considered than for monocomponent systems. Also, concentration effects were relatively more destabilizing in the cylindrical geometry with a lateral wall in which the temperature profile remained fixed, i.e. a so-called conducting lateral wall, than in the Bénard geometry. Contrary to the expectations of Ybarra and Velarde[25] and Gutkowicz-Krusin *et al.*,[27] but in apparent agreement with Crespo and Velarde,[29] Abernathey and Rosenberger determined that the

contribution of the Dufour effect to the stability of these systems was quite minor compared to that of the Soret effect. They estimated that the error in the critical Rayleigh number ($R\tilde{a}^c$) which would result from neglecting the Dufour effect would be a maximum of 5% for the Xe–He system and much less for the Xe–Ar system.

In addition to the array of interesting concentration effects which have been observed in binary systems, the cylinder aspect ratio also plays a critical role in affecting flow structure at the onset of convection; however, the available experimental data regarding the variation of the cylinder aspect ratio focus almost exclusively on monocomponent systems. A variety of different roll cell structures have been observed for monocomponent systems near the onset of convection in cylinders of moderate radius-to-height ratios ($\gamma \equiv R/L$). For example, Mitchell and Quinn[34] observed both axisymmetric and non-axisymmetric flows in cylinders with aspect ratios near one ($\gamma \approx 1$). Similarly, Stork and Müller[35] observed numerous different flow patterns near the onset of convection in cylinders with moderate aspect ratios.

The goal of this study is to provide a detailed analysis of the mechanism of the inception and sustenance of flows of binary mixtures (including the limiting case of monocomponent fluids) in vertical cylinders, and of observed flow structure at its onset. In particular, the effects of varying the aspect ratio of the cylinder and composition of the fluid are considered. This study complements that of Crespo and Velarde[29] by presenting a more quantitative analysis of both steady and oscillatory flows, from which additional physical insight can be gleaned. (Oscillatory stability and weakly non-linear effects will be discussed in subsequent papers.)

2. MATHEMATICAL DESCRIPTION

The system to be studied consists of a layer of non-reactive fluid which fills a vertical, circular cylindrical container heated from below. Both monocomponent fluids and binary mixtures are considered. Assuming that the temperature and concentration gradients are small, as required by the Boussinesq approximation, the diffusive heat and mass fluxes $\mathbf{q}$ and $\mathbf{j}_1$ (mass flux of species 1) are given by[4]

$$\text{heat:} \quad -\mathbf{q} = k\nabla T + \bar{\rho}_1 \mu_1^{W_1} \bar{T} D'' \nabla W_1, \tag{1}$$

$$\text{mass:} \quad -\mathbf{j}_1 = \bar{\rho} D' \bar{W}_1 \bar{W}_2 \nabla T + \bar{\rho} D \nabla W_1, \tag{2}$$

where $\bar{T}$ and $\bar{\rho}$ are the volume-averaged temperature and density respectively; $\bar{\rho}_1$ is the volume-averaged density of component 1; $\mu_1^{W_1}$ is the partial derivative of the chemical potential of component 1 with respect to W_1, its mass fraction; $\bar{W}_1$ and $\bar{W}_2$ are the volume-averaged mass fractions of the two components; k is the thermal conductivity; D is the mass diffusivity; and D'' and D' are the Dufour and Soret 'diffusion' coefficients respectively. Here component 1 will be taken to be the denser component. These forms of the phenomenological transport equations directly illustrate the coupling of the Soret and Dufour effects since, from Onsager's reciprocal relations,[36,37] $D' = D''$.

It is convenient to use the cylindrical co-ordinate system shown in Figure 1 with the gravitational field anti-parallel to the z-axis, in the mathematical characterization of the system. The entire boundary of the region is assumed to be a rigid, no-slip boundary which is impermeable to the fluid but not necessarily to heat. The temperature profile is initially vertical and linear (for the conduction state), with temperature T_T on the upper boundary and T_B on the lower boundary; the initial concentration profile is similar, with concentrations W_T and W_B such that Soret diffusion balances ordinary diffusion. Even though the system is closed with respect to mass, a gradient in concentration is induced by the Soret effect, which, along with the Dufour

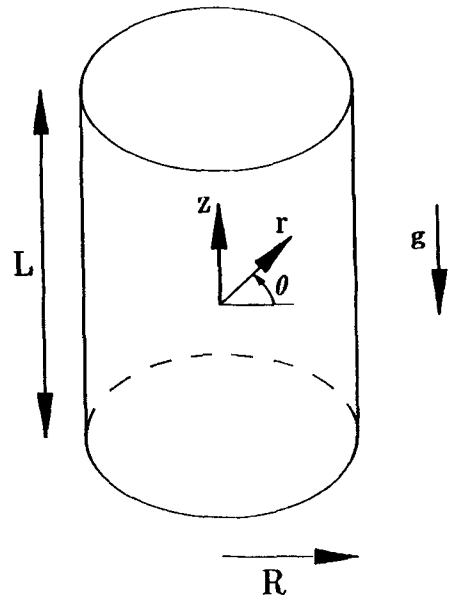

Figure 1. Problem geometry and co-ordinate system

effect, couples the temperature and concentration fields. These effects can be either stabilizing or destabilizing.

The thermal conductivity (k), the mass diffusivity (D), the Soret and Dufour coefficients (D' and D''), the heat capacity (C_p), the viscosity (μ and $\mu_1^{W_1}$) are assumed constant and are evaluated at $\bar{\rho}$, $\bar{T}$ and W_1 for the conduction state. The density of the fluid (ρ) is assumed to be a linear function of temperature and composition. In terms of dimensional variables, the equation of state is

$$\rho = \bar{\rho}[1 - \alpha(T - \bar{T}) + \beta(W_1 - \bar{W}_1)], \tag{3}$$

where

$$\alpha \equiv \left(-\frac{1}{\rho}\frac{\partial \rho}{\partial T} \right)_{T=\bar{T}}, \qquad \beta \equiv \left(\frac{1}{\rho}\frac{\partial \rho}{\partial W_1} \right)_{W_1 = \bar{W}_1} \tag{4}$$

are the thermal and solutal expansion coefficients respectively. Making use of the Boussinesq approximation[38–40] leads to the following non-dimensional equations for determining the dimensionless velocity ($\mathbf{u}$), pressure (p), temperature (T) and 'concentration' (η):

$$\frac{\partial \mathbf{u}}{\partial t} + \mathbf{u}\cdot\nabla\mathbf{u} = -\nabla p + (T - \psi\eta)\mathbf{e}_z + \nabla^2\mathbf{u}, \tag{5}$$

$$\tilde{Pr}\left(\frac{\partial T}{\partial t} + \mathbf{u}\cdot\nabla T \right) = \nabla^2 T + \zeta\nabla^2\eta + \tilde{Ra}\mathbf{e}_z\cdot\mathbf{u}, \tag{6}$$

$$\tilde{Sc}\left(\frac{\partial \eta}{\partial t} + \mathbf{u}\cdot\nabla\eta \right) = \nabla^2 T + \nabla^2\eta, \tag{7}$$

$$\nabla\cdot\mathbf{u} = 0, \tag{8}$$

where $\tilde{Ra}$, $\tilde{Pr}$ and $\tilde{Sc}$ are the Rayleigh, Prandtl and Schmidt numbers respectively, ψ and ζ are

parameters related to the Soret and Dufour effects respectively and $\mathbf{e}_z$ is the vertical unit vector. (Note that here and hereafter T represents a dimensionless variable.) The new variable η was introduced to simplify the form of the boundary conditions and will be discussed further shortly. Here $\tilde{Ra}$, $\tilde{Pr}$ and $\tilde{Sc}$ are defined appropriately for a binary mixture as

$$\tilde{Ra} \equiv \frac{gL^3\bar{\alpha}\Delta T}{\nu\alpha_1}, \qquad \tilde{Pr} \equiv \frac{\nu}{\alpha_1}, \qquad \tilde{Sc} \equiv \frac{\nu}{\beta_2}, \tag{9}$$

where g is the gravitational acceleration, L is the height of the cylinder, $\Delta T \equiv T_B - T_T$ and $\nu \equiv \mu/\bar{\rho}$ is the kinematic viscosity. Also $\bar{\alpha}$, α_1 and β_2 are the thermal expansion coefficient, thermal diffusivity and mass diffusivity respectively, modified appropriately for the non-dimensionalization used here for a binary system, and are given by

$$\bar{\alpha} \equiv \alpha\left(1 + \frac{\beta\gamma_2}{\alpha D}\right), \qquad \alpha_1 \equiv \kappa\left(1 - \frac{\gamma_1\gamma_2}{\kappa D}\right), \qquad \beta_2 \equiv D\left(1 + \frac{\gamma_1\gamma_2}{D^2}\right), \tag{10}$$

where $\kappa \equiv k/\bar{\rho}C_p$ is the thermal diffusivity and γ_1 and γ_2 are modified Dufour and Soret coefficients defined by

$$\gamma_1 \equiv \frac{1}{C_p}\bar{W}_1\mu_1^{W_1}\bar{T}D'', \qquad \gamma_2 \equiv \bar{W}_1\bar{W}_2D'. \tag{11}$$

The dimensionless time t, velocity $\mathbf{u}$, temperature T and pressure p are defined as follows, using a superscript 'd' to denote the *dimensional* variables (η will be defined shortly):

$$t \equiv \frac{t^d}{L^2/\nu}, \qquad \mathbf{u} \equiv \frac{\mathbf{u}^d}{\nu/L}, \qquad T \equiv \frac{T^d}{\nu^2/gL^3\bar{\alpha}}, \qquad p \equiv \frac{p^d}{\bar{\rho}\nu^2/L^2}. \tag{12}$$

The Soret and Dufour parameters ψ and ζ are defined as

$$\psi \equiv \frac{\beta\gamma_2\alpha_1}{\beta_2\bar{\alpha}D} = \frac{\kappa}{D}\left(\frac{S}{1+S}\right)F_D, \qquad \zeta \equiv 1 - \frac{D}{\beta_2} = \frac{(\kappa/D)(1-F_D)}{\kappa/D+1}, \tag{13}$$

where

$$F_D \equiv \frac{1-\gamma_1\gamma_2/\kappa D}{1+\gamma_1\gamma_2/D^2}, \qquad S \equiv \frac{\beta k_T^{mass}}{\alpha\bar{T}} = \frac{\beta\gamma_2}{\alpha D}. \tag{14}$$

The parameter S is the so-called 'Soret separation number', where k_T^{mass} is the (mass) thermal diffusion ratio used, for example, by de Groot and Mazur.[4] The thermal diffusion ratio is proportional to the ratio of the Soret diffusion coefficient to the mass diffusivity and is defined as

$$k_T^{mass} \equiv \bar{W}_1\bar{W}_2\bar{T}\frac{D'}{D}. \tag{15}$$

The physical parameters g, $\bar{\alpha}$, μ, ν, α_1, β_2, β_1, α, D, κ, γ_1, γ_2, C_p, $\mu_1^{W_1}$, ψ, ζ, S, k_T^{mass} and F_D are all assumed to be constant and are evaluated at $\bar{\rho}$, $\bar{W}_1$ and $\bar{T}$. The values of ψ and ζ used for the Xe–He and Xe–Ar mixtures studied herein can be obtained from tables given in Abernathey and Rosenberger.[28] The values for other systems are given in the text. Clearly the relationships between the various parameters used in the literature are rather involved, but enough information is provided here to relate the parameters used in this study to those used in other works. The non-dimensionalization was discussed in detail by Hardin.[33] It is noteworthy that the Rayleigh, Prandtl and Schmidt numbers defined above reduce to the standard definitions for mono-component fluids when ψ and ζ are zero.

Two separate length scales are used to non-dimensionalize the radial and vertical co-ordinates, namely the radius R and height L of the cylinder respectively. This gives

$$r \equiv \frac{r^{\mathrm{d}}}{R}, \qquad z \equiv \frac{z^{\mathrm{d}}}{L}. \tag{16}$$

The appropriate definitions of the differential operators are as follows:

$$\nabla s \equiv \mathbf{e}_r \gamma^{-1} \frac{\partial s}{\partial r} + \mathbf{e}_\theta (r\gamma)^{-1} \frac{\partial s}{\partial \theta} + \mathbf{e}_z \frac{\partial s}{\partial z}, \tag{17}$$

$$\nabla^2 s \equiv r^{-1}\gamma^{-2} \frac{\partial}{\partial r}\left(r \frac{\partial s}{\partial r}\right) + (r\gamma)^{-2} \frac{\partial^2 s}{\partial \theta^2} + \frac{\partial^2 s}{\partial z^2}, \tag{18}$$

$$\nabla \cdot \mathbf{v} \equiv (r\gamma)^{-1} \frac{\partial}{\partial r}(r v_r) + (r\gamma)^{-1} \frac{\partial v_\theta}{\partial \theta} + \frac{\partial v_z}{\partial z}, \tag{19}$$

$$\begin{aligned} \nabla^2 \mathbf{v} \equiv & \left[\gamma^{-2} \frac{\partial}{\partial r}\left(r^{-1} \frac{\partial}{\partial r}(r v_r)\right) + (r\gamma)^{-2} \frac{\partial^2 v_r}{\partial \theta^2} - 2(r\gamma)^{-2} \frac{\partial v_\theta}{\partial \theta} + \frac{\partial^2 v_r}{\partial z^2} \right] \mathbf{e}_r \\ & + \left[\gamma^{-2} \frac{\partial}{\partial r}\left(r^{-1} \frac{\partial}{\partial r}(r v_\theta)\right) + (r\gamma)^{-2} \frac{\partial^2 v_\theta}{\partial \theta^2} + 2(r\gamma)^{-2} \frac{\partial v_r}{\partial \theta} + \frac{\partial^2 v_\theta}{\partial z^2} \right] \mathbf{e}_\theta \\ & + \left[r^{-1}\gamma^{-2} \frac{\partial}{\partial r}\left(r \frac{\partial v_z}{\partial r}\right) + (r\gamma)^{-2} \frac{\partial^2 v_z}{\partial \theta^2} + \frac{\partial^2 v_z}{\partial z^2} \right] \mathbf{e}_z, \end{aligned} \tag{20}$$

where s is any scalar, $\mathbf{v}$ is any vector and $\mathbf{e}_r$, $\mathbf{e}_\theta$, $\mathbf{e}_z$ are the unit vectors of cylindrical co-ordinate system. Note that the use of two length scales in the non-dimensionalization leads to the appearance of an aspect ratio $\gamma \equiv R/L$ in the differential operators, where R and L are the radius and height of the cylinder respectively, but conveniently sets the range of the deimensionless independent variables to be $[0, 1]$ for r and $[-\frac{1}{2}, \frac{1}{2}]$ for z in all cases.

Two different sets of boundary conditions are utilized:

$$\mathbf{u} = 0,\ T = 0,\ \mathbf{n}\cdot\nabla\eta = 0 \qquad \text{on} \quad r = 1,\ -\tfrac{1}{2} \leqslant z \leqslant \tfrac{1}{2}, \tag{21}$$

$$\mathbf{u} = 0,\ T = 0,\ \mathbf{n}\cdot\nabla\eta = 0 \qquad \text{on} \quad 0 \leqslant r \leqslant 1,\ z = \pm\tfrac{1}{2}, \tag{22}$$

and

$$\mathbf{u} = 0,\ \mathbf{n}\cdot\nabla T = 0,\ \mathbf{n}\cdot\nabla\eta = 0 \qquad \text{on} \quad r = 1,\ -\tfrac{1}{2} \leqslant z \leqslant \tfrac{1}{2}, \tag{23}$$

$$\mathbf{u} = 0,\ T = 0,\ \mathbf{n}\cdot\nabla\eta = 0 \qquad \text{on} \quad 0 \leqslant r \leqslant 1,\ z = \pm\tfrac{1}{2}. \tag{24}$$

The first corresponds to so-called thermally *conducting* boundaries everywhere, while the second corresponds to thermally conducting top and bottom boundaries and an *insulating* lateral boundary. (Here *conducting* implies that the value of the variable is specified (a Dirichlet condition), and *insulating* implies that the derivative of the variable normal to the boundary is specified (a Neumann condition).) A new composite variable η whose dimensional form is

$$\eta^{\mathrm{d}} \equiv W_1^{\mathrm{d}} + \left(\frac{\bar{W}_1 \bar{W}_2 D'}{D} \right) T^{\mathrm{d}} \tag{25}$$

has been introduced to simplify the fomulation by decoupling the boundary conditions. The zero-mass-flux boundary condition $D\mathbf{n}\cdot\nabla W_1 + \bar{W}_1 \bar{W}_2 D' \mathbf{n}\cdot\nabla T = 0$ becomes $\mathbf{n}\cdot\nabla\eta = 0$. Note that the dependent variables as defined here are deviations from the quiescent base state in which the

temperature and concentration vary linearly with z, such that η is constant, and the pressure is hydrostatic.

Unlike the thermal and mass diffusivities, the Dufour and Soret coefficients $D'' = D'$, to which ζ and ψ are related, may be either positive or negative depending on the specific species chosen as component 1, since the mass fraction of species 1 is the chosen concentration variable. Note that D' for component 2 is the negative of D' for component 1. As given in equation (7), the species mass balance has been recast in terms of η, but it is a balance equation for component 1. Therefore, when D' is positive, species 1 will tend to move towards the colder region. Conversely, when D' is negative, component 1 will move towards the warmer region. Hence the Soret effect will be destabilizing when $D' > 0$ with component 1 being the denser component (i.e. the component for which $\beta > 0$, β being the solutal expansion coefficient defined previously) and the fluid mixture is heated from below. Analogously, when $D'' > 0$, the Dufour effect will yield an energy flux towards the region with a lower concentration of component 1. The Dufour effect will be destabilizing when $D'' > 0$ if the concentration of species 1 is lower at the bottom of the fluid layer. The contribution of the Dufour effect is thus seen to be directly coupled to the Soret effect.

It should be emphasized that the higher-molecular-weight species is not always the *denser* component. For example, in water–alcohol mixtures, water is typically the denser constituent, even though it has the lower molecular weight. Thus if component 1 is the alcohol, one might expect the solutal expansion coefficient (β) to be negative since our equation of state is based on the local weight fraction of species 1. The sign of β enters the non-dimensional stability problem through ψ because of the dependence of ψ on S. As noted by Schechter *et al.*,[13] S represents the ratio of the contribution to the density gradient from the Soret effect to that from thermal expansion, as seen from

$$S = \frac{\beta \bar{W}_1 \bar{W}_2 D'}{\alpha D}. \tag{26}$$

Thus when β changes sign, so does S. Consequently, a system for which $\beta < 0$ and $D' < 0$ will behave similarly to a system for which $\beta > 0$ and $D' > 0$, assuming that α has the same sign in both cases. (With α as previously defined, usually $\alpha > 0$.) When heating is from below, the Soret effect will tend to destabilize both cases, as expected, since in both cases the *denser* species will preferentially migrate towards the top.

It is also necessary to clarify the relationship between S, which has a clear physical interpretation, and ψ, which is the particular form of the dimensionless Soret coefficient that arises in the governing equations (5)–(8) for the non-dimensionalization used here. When $S = -1$, the contribution to the density gradient from the Soret effect exactly balances the contribution to the density gradient from the temperature gradient. As seen from the definition of ψ, the limit of $\psi \to -\infty$ corresponds to $S \to -1$ from *above*, i.e. from greater S. The case of $S \to -1$ from *below* corresponds to *positive* ψ. While this may seem paradoxical at first glance, recall that

$$\tilde{Ra} \equiv \frac{gL^3 \bar{\alpha} \Delta T}{\nu \alpha_1}, \qquad \bar{\alpha} \equiv \alpha\left(1 + \frac{\beta \gamma_2}{\alpha D}\right) = \alpha(1 + S).$$

If $S < -1$, then $\bar{\alpha} < 0$, and $\tilde{Ra}$ is thus *negative for heating from below* and *positive for heating from above*, assuming, as is probable, that $\alpha > 0$. As $S \to -1$, so that $\nabla\rho \to 0$, then $\bar{\alpha} \to 0$, so that in order to drive convection, $|\Delta T| \to \infty$, as expected. Thus the entire parameter range of S is appropriately described, although the relationship between S and ψ is not intuitive. Furthermore, fluids with $\alpha < 0$ are also represented as long as the linear dependence of ρ on T is appropriate. Finally, a somewhat ambiguous statement by Gutkowicz-Krusin *et al.*[26] relating to the physical meaning of ψ is brought to the reader's attention. These authors stated that " . . . $\psi \equiv \beta\alpha_2/\bar{\alpha}\beta_2$ is

positive for the 'normal' Soret effect . . . " having previously stated that " . . . the 'normal' Soret effect occurs when the concentration of the component of higher molecular weight is higher in the colder region". However, for the higher-molecular-weight component to prefer the colder region, it is only necessary that $\gamma_2 > 0$ (i.e. $D' > 0$) for that component, which does not necessarily make ψ positive since either β or $\bar{\alpha} = \alpha(1 + S)$ could be negative. This clarification is important since there are many binary fluid mixtures for which $\beta < 0$ if the equation of state is based on the higher-molecular-weight component. (The parameter α_2 is defined by

$$\alpha_2 \equiv \frac{\gamma_2}{D}\alpha_1 = \frac{\gamma_2 \kappa}{D}\left(1 - \frac{\gamma_1 \gamma_2}{\kappa D}\right) \tag{27}$$

and will have the same sign as γ_2 since $0 \leq \gamma_1 \gamma_2 / \kappa D \leq 1$. The inequalities result from Onsager's reciprocal relations and the second law of thermodynamics.[4] Also recall that γ_1 and γ_2 are related to D'' and D'.)

3. LINEAR STABILITY PROBLEM

3.1. Formulation of the problem

In order to gain some valuable insight into the mechanism of destabilization and point of incipient flow in the system, one first considers the associated linear stability problem. Formally, it is obtained from equations (5)–(8) by linearizing them about the quiescent base state and then seeking solutions with exponential time dependence:

$$\mathbf{u}: \ \mathbf{U}(r, z, \theta)e^{\sigma t}, \tag{28}$$

$$T: \ \Theta(r, z, \theta)e^{\sigma t}, \tag{29}$$

$$\eta: \ \Gamma(r, z, \theta)e^{\sigma t}, \tag{30}$$

$$p: \ P(r, z, \theta)e^{\sigma t}, \tag{31}$$

where $\sigma = \sigma_r + i\sigma_i$, $i \equiv \sqrt{(-1)}$, is a complex amplification factor. In general, $\mathbf{U}$, Θ, Γ and P are complex-valued functions. Substitution into equations (5)–(8) leads to

$$\nabla^2 \mathbf{U} + (\Theta - \psi\Gamma)\mathbf{e}_z - \nabla P = \sigma \mathbf{U}, \tag{32}$$

$$\nabla^2 \Theta + \zeta \nabla^2 \Gamma + \tilde{Ra}\mathbf{e}_z \cdot \mathbf{U} = \tilde{Pr}\sigma\Theta, \tag{33}$$

$$\nabla^2 \Theta + \nabla^2 \Gamma = \tilde{Sc}\sigma\Gamma, \tag{34}$$

$$\nabla \cdot \mathbf{U} = 0, \tag{35}$$

with either

$$\mathbf{U} = 0, \Theta = 0, \mathbf{n} \cdot \nabla\Gamma = 0 \quad \text{on} \quad r = 1, -\tfrac{1}{2} \leq z \leq \tfrac{1}{2}, \tag{36}$$

$$\mathbf{U} = 0, \Theta = 0, \mathbf{n} \cdot \nabla\Gamma = 0 \quad \text{on} \quad 0 \leq r \leq 1, z = \pm\tfrac{1}{2}, \tag{37}$$

or

$$\mathbf{U} = 0, \mathbf{n} \cdot \nabla\Theta = 0, \mathbf{n} \cdot \nabla\Gamma = 0 \quad \text{on} \quad r = 1, -\tfrac{1}{2} \leq z \leq \tfrac{1}{2}, \tag{38}$$

$$\mathbf{U} = 0, \Theta = 0, \mathbf{n} \cdot \nabla\Gamma = 0 \quad \text{on} \quad 0 \leq r \leq 1, z = \pm\tfrac{1}{2}. \tag{39}$$

The solutions $(\mathbf{U}, \Theta, \Gamma, P)$ of equations (32)–(39) separate into two classes, one even and the other odd about $z = 0$ with respect to the temperature, concentration and vertical velocity fields;

the radial velocity, azimuthal velocity and pressure have the opposite (odd or even) symmetry.[41] This property will be utilized in the approximate solution of the system by means of Galerkin's method by employing two sets of basis functions with the proper even and odd properties for each field.

3.2. Solution of the linear stability problem: Galerkin's technique

Even though the linear stability problem represents a linear mathematical system, an analytical solution cannot be obtained by separation of variables because of the no-slip condition at the container walls. However, the problem does simplify to a series of uncoupled 'modal' solutions in the azimuthal co-ordinate, with each solution having an angular dependence derived from $e^{-in\theta}$. Each mode corresponds to a different value of n, where n represents the number of azimuthal dividing planes in the solution, i.e. vertical planes through $r = 0$ on which the azimuthal velocity is zero. This decoupling in the azimuthal co-ordinate has a direct effect on the numerical solution, which will be evident shortly.

Since no analytical solution is available, Galerkin's method[42] is employed here to generate an approximate solution of desired accuracy. This method projects the mathematical problem from an appropriate infinite-dimensional function space to a finite-dimensional subspace on which the solution of the problem reduces to that of an algebraic eigenvalue problem. Following this approach, a finite series representation for each variable ($\mathbf{U}$, P, Θ, Γ) is chosen to be of the general form

$$\mathbf{U} = \sum_{j,k} \mathbf{U}_{jkn} = \sum_{j,k} (A_{jkn}\mathbf{V}_{jkn} + D_{jkn}\mathbf{W}_{jkn}) \quad \text{(3D)} \tag{40}$$

or

$$\mathbf{U} = \sum_{j,k} \mathbf{U}_{jk0} = \sum_{j,k} A_{jk0}\mathbf{O}_{jk0} \text{ (2D axisymmetric)}, \tag{41}$$

and

$$\Theta = \sum_{j,k} \Theta_{jkn} = \sum_{j,k} B_{jkn}\Phi_{jkn}, \tag{42}$$

$$\Gamma = \sum_{j,k} \Gamma_{jkn} = \sum_{j,k} C_{jkn}\Lambda_{jkn}, \tag{43}$$

$$P = \sum_{j,k} P_{jkn} = \sum_{j,k} E_{jkn}\Pi_{jkn}, \tag{44}$$

where $\mathbf{V}_{jkn}$ and $\mathbf{W}_{jkn}$ or $\mathbf{O}_{jk0}$ are the velocity basis functions for 3D and 2D flows respectively and Φ_{jkn}, Λ_{jkn} and Π_{jkn} are the temperature, 'concentration' (η) and pressure basis functions respectively. The value of n denotes the particular modal solution and hence determines the azimuthal symmetry as described at the beginning of this subsection. Note that $n = 0$ corresponds to the axisymmetric case. The velocity is a vector field and hence is expectedly more complex than the other, scalar fields; moreover, it is required to be solenoidal, which places additional constraints on its form. The form of the basis functions $\mathbf{V}_{jkn}$, $\mathbf{W}_{jkn}$, $\mathbf{O}_{jk0}$, Φ_{jkn}, Λ_{jkn} and Π_{jkn} must be specified before these representations can be utilized; according to Galerkin's method, these basis functions are chosen such that the essential boundary conditions are satisfied. Essential boundary conditions in a problem such as this are the specification of the velocity, temperature and concentration on the boundary plus necessary boundedness properties. The specification of

stresses or fluxes amounts to natural boundary conditions and need not be satisfied explicitly. Nevertheless, in this analysis these conditions are also satisfied explicitly by the chosen basis functions.

Since the velocity field must be solenoidal, it is clear that $\mathbf{U}_{jkn}$ must be solenoidal. Consequently, it is convenient to choose $\mathbf{V}_{jkn}$, $\mathbf{W}_{jkn}$ and $\mathbf{O}_{jk0}$ to be solenoidal. Since the divergence of the curl of any vector is zero, this can be done by expressing these functions in terms of vector potentials, specifically

$$\mathbf{V}_{jkn} = \nabla \times (\phi_{jkn}\mathbf{e}_r), \tag{45}$$

$$\mathbf{W}_{jkn} = \nabla \times (\zeta_{jkn}\mathbf{e}_z), \tag{46}$$

$$\mathbf{O}_{jk0} = \nabla \times (\psi_{jk0}\mathbf{e}_\theta). \tag{47}$$

The axisymmetric velocity basis functions are derived from a streamfunction ψ_{jk0}, while the non-axisymmetric velocity basis functions are derived from two scalar functions ϕ_{jkn} and ζ_{jkn} in such a way that their combination will represent a general three-dimensional solenoidal velocity field. The resulting form of the velocity field will be discussed shortly.

To obtain the solution using a minimal number of orthogonal basis functions for each variable requires judicious regard of the geometry of the problem. The radial behaviour of the basis functions should be well suited to the cylindrical sidewall, while the vertical behaviour should reflect the flat, parallel upper and lower bounding surfaces. The field representations used in this analysis for the axisymmetric case are an augmentation of those used by Charlson and Sani,[41,43] who studied the stability of a monocomponent fluid in a rigid cylindrical geometry heated from below, in order to allow the consideration of a binary fluid mixture. For non-axisymmetric solutions the chosen field representations are an augmentation of those used by Buell and Catton,[44] who studied the same problem as Charlson and Sani[43] but employed different basis functions. The representation (45)–(47) used herein is supported by the study of Crespo *et al.*[45] The similarity of the energy and species mass balance equations (33) and (34) suggests that similar basis functions be used for these fields. Furthermore, the homogeneous boundary conditions on Γ on the sidewall are identical in form to those for the temperature field in a cylinder with a thermally insulating sidewall. Hence the representation for the η-field is conveniently chosen to be that used by Charlson and Sani for a cylinder with an insulating sidewall, except that the trial function for the η-field must be *insulating* rather than *conducting* on the top and bottom of the cylinder as well as on the sidewall. Finally, the velocity representations used by Charlson and Sani for the axisymmetric case, or by Buell and Catton for the non-axisymmetric case, are appropriate without change for this analysis. Thus the field representations used in this study are either those of equations (41)–(44) or equations (40) and (42)–(44) utilizing the following basis functions.

Velocity

Axisymmetric case

$$\mathbf{O}_{jk0} \equiv \left\{ \frac{1}{r} Y_k X_j' \mathbf{e}_r - \frac{1}{\gamma r} Y_k' X_j \mathbf{e}_z \right\}, \tag{48}$$

where Y_k and X_j are the radial (r) and vertical (z) basis functions given by

$$Y_k(r) \equiv r[J_{n+1}(\lambda_k r) + \beta_k I_{n+1}(\lambda_k r)], \tag{49}$$

$$\beta_k \equiv \frac{-J_{n+1}(\lambda_k)}{I_{n+1}(\lambda_k)}, \tag{50}$$

where λ_k is the kth root of

$$J_n(\lambda_k)I_{n+1}(\lambda_k) - J_{n+1}(\lambda_k)I_n(\lambda_k) = 0, \tag{51}$$

and

$$X_j(z) \equiv \frac{\cosh(\mu_j z)}{\cosh(\frac{1}{2}\mu_j)} - \frac{\cos(\mu_j z)}{\cos(\frac{1}{2}\mu_j)}, \tag{52}$$

where μ_j is the jth root of

$$\tanh(\tfrac{1}{2}\mu_j) + \tan(\tfrac{1}{2}\mu_j) = 0 \tag{53}$$

for an 'even' trial function, or

$$X_j(z) \equiv \frac{\sinh(\mu_j z)}{\sinh(\frac{1}{2}\mu_j)} - \frac{\sin(\mu_j z)}{\sin(\frac{1}{2}\mu_j)}, \tag{54}$$

where μ_j is the j-th root of

$$\coth(\tfrac{1}{2}\mu_j) - \cot(\tfrac{1}{2}\mu_j) = 0 \tag{55}$$

for an 'odd' trial function. Here a prime ($'$) denotes differentiation with respect to the independent variable r or z. The definitions of β_k, λ_k and μ_j are chosen such that Y_k, X_j, Y_k' and X_j' are all zero at the boundaries in order to satisfy the conditions of zero velocity at the boundaries. Henceforth, for convenience in describing the spatial structure of a particular modal solution (i.e. a solution for a particular value of n), the terms 'even' and 'odd' will be used to describe the symmetry of the mode across the horizontal midplane with respect to its temperature, concentration and vertical velocity.

Non-axisymmetric case

$$\mathbf{V}_{jkn} \equiv \left\{ X_j' J_{n+1}(\delta_k r)\sin(n\theta)\mathbf{e}_\theta - \frac{n}{\gamma} X_j \frac{1}{r} J_{n+1}(\delta_k r)\cos(n\theta)\mathbf{e}_z \right\}, \tag{56}$$

$$\mathbf{W}_{jkn} \equiv \left\{ \frac{n}{\gamma}\sin(2j\pi z)\frac{1}{2}R_k\cos(n\theta)\mathbf{e}_r - \frac{1}{\gamma}R_k'\sin(2j\pi z)\sin(n\theta)\mathbf{e}_\theta \right\} \tag{57}$$

for an 'even' case, with X_j defined by equations (52) and (53). For an 'odd' case X_j will be given by equations (54) and (55), and the function $\sin(2j\pi z)$ is replaced by $\cos[(2j-1)\pi z]$. The radial basis function R_k is defined as

$$R_k(r) \equiv \frac{J_n(\omega_k r)}{J_n(\omega_k)} - \frac{I_n(\omega_k r)}{I_n(\omega_k)}, \tag{58}$$

where ω_k is the kth root of the equation

$$J_n(\omega_k)I_{n+1}(\omega_k) + I_n(\omega_k)J_{n+1}(\omega_k) = 0. \tag{59}$$

Finally, δ_k is the kth root of $J_{n+1}(\delta_k r) = 0$. The definitions of δ_k and ω_k are chosen such that $J_{n+1}(\delta_k r)$, R_k and R_k' are all zero at the sidewall in order to satisfy the condition of zero velocity there. The conditions of zero velocity at the top and bottom of the container are satisfied by the vertical basis functions by construction, as for the axisymmetric case.

Temperature

$$\Phi_{jkn} \equiv \cos[(2j-1)\pi z]J_n(\alpha_k r)\cos(n\theta) \tag{60}$$

for an 'even' case, or

$$\Phi_{jkn} \equiv \sin(2j\pi z) J_n(\alpha_k r)\cos(n\theta) \tag{61}$$

for an 'odd' case. Here α_k is the kth root of J_n for a cylinder with a conducting sidewall in order to satisfy the condition of zero temperature perturbation at the sidewall, or the kth root of J_n' for a cylinder with an insulating sidewall in order to satisfy the condition of zero radial derivative of the temperature at the sidewall. The conditions of zero temperature perturbation at the top and bottom of the cylinder are obviously satisfied by construction.

η-Field

$$\Lambda_{jkn} \equiv \cos(2j\pi z) J_n(\alpha_k^{\#} r)\cos(n\theta) \tag{62}$$

for an 'even' case (starting with $j = 0$), or

$$\Lambda_{jkn} \equiv \sin[(2j-1)\pi z] J_n(\alpha_k^{\#} r)\cos(n\theta) \tag{63}$$

for an 'odd' case. Here $\alpha_k^{\#}$ is the kth root of J_n' so that the condition of zero mass flux through the sidewall is satisfied. The impermeability of the top and bottom of the cylinder is obviously satisfied by construction.

It is noteworthy that the pressure representation is not specified, since the pressure is conveniently eliminated from the Galerkin formulation via constraints imposed on the basis function by the continuity equation, and hence no specific representation is required. With the field representations thus specified, the Galerkin formulation of the problem can now be developed.

Galerkin's technique can now be formally applied to generate the finite-dimensional approximation alluded to earlier in this subsection by requiring the projection of the *residual function* associated with each balance equation (32)–(35) to be orthogonal to each of the appropriate basis functions. In the present case it is appropriate to use an L_2 inner product to define the projection. That is, $\langle \mathbf{f}, \mathbf{g} \rangle \equiv \int_\Omega \tilde{\mathbf{f}} \cdot \mathbf{g}\, d\Omega$, where Ω is the domain of interest and $\tilde{\mathbf{f}}$ is the complex conjugate of the function $\mathbf{f}$. The obvious scalar equivalent is denoted by the same $\langle , \rangle$ notation for simplicity. Thus, for the axisymmetric case ($n = 0$),

$$\sum_{j,k} \{ -\sigma \langle \mathbf{O}_{rs0}, \mathbf{U}_{jk0} \rangle + \langle \mathbf{O}_{rs0}, \nabla^2 \mathbf{U}_{jk0} \rangle - \langle \mathbf{O}_{rs0}, \nabla P_{jk0} \rangle + \langle \mathbf{O}_{rs0}, (\Theta_{jk0} \mathbf{e}_z) \rangle - \psi \langle \mathbf{O}_{rs0}, (\Gamma_{jk0} \mathbf{e}_z) \rangle \} = 0, \tag{64}$$

$$\sum_{j,k} \{ -\sigma \tilde{Pr} \langle \Phi_{rs0}, \Theta_{jk0} \rangle + \langle \Phi_{rs0}, \nabla^2 \Theta_{jk0} \rangle + \zeta \langle \Phi_{rs0}, \nabla^2 \Gamma_{jk0} \rangle + \tilde{Ra}_0 \langle \mathbf{U}_{jk0}, (\Phi_{rs0} \mathbf{e}_z) \rangle \} = 0, \tag{65}$$

$$\sum_{j,k} \{ -\sigma \tilde{Sc} \langle \Lambda_{rs0}, \Gamma_{jk0} \rangle + \langle \Lambda_{rs0}, \nabla^2 \Theta_{jk0} \rangle + \langle \Lambda_{rs0}, \nabla^2 \Gamma_{jk0} \rangle \} = 0; \tag{66}$$

while for a non-axisymmetric case ($n \neq 0$),

$$\sum_{j,k} \{ -\sigma \langle \mathbf{V}_{rsn}, \mathbf{U}_{jkn} \rangle + \langle \mathbf{V}_{rsn}, \nabla^2 \mathbf{U}_{jkn} \rangle - \langle \mathbf{V}_{rsn}, \nabla P_{jkn} \rangle + \langle \mathbf{V}_{rsn}, (\Theta_{jkn} \mathbf{e}_z) \rangle - \psi \langle \mathbf{V}_{rsn}, (\Gamma_{jkn} \mathbf{e}_z) \rangle \} = 0, \tag{67}$$

$$\sum_{j,k}\{-\sigma\langle \mathbf{W}_{rsn}, \mathbf{U}_{jkn}\rangle + \langle \mathbf{W}_{rsn}, \nabla^2 \mathbf{U}_{jkn}\rangle - \langle \mathbf{W}_{rsn}, \nabla P_{jkn}\rangle + \langle \mathbf{W}_{rsn}, (\Theta_{jkn}\mathbf{e}_z)\rangle - \psi\langle \mathbf{W}_{rsn}, (\Gamma_{jkn}\mathbf{e}_z)\rangle\} = 0, \tag{68}$$

$$\sum_{j,k}\{-\sigma \tilde{Pr}\langle \Phi_{rsn}, \Theta_{jkn}\rangle + \langle \Phi_{rsn}, \nabla^2 \Theta_{jkn}\rangle + \zeta\langle \Phi_{rsn}, \nabla^2 \Gamma_{jkn}\rangle + \tilde{Ra}_n\langle \mathbf{U}_{jkn}, (\Phi_{rsn}\mathbf{e}_z)\rangle\} = 0, \tag{69}$$

$$\sum_{j,k}\{-\sigma \tilde{Sc}\langle \Lambda_{rsn}, \Gamma_{jkn}\rangle + \langle \Lambda_{rsn}, \nabla^2 \Theta_{jkn}\rangle + \langle \Lambda_{rsn}, \nabla^2 \Gamma_{jkn}\rangle\} = 0. \tag{70}$$

Here r and s are particular values of j and k respectively. Equations (64)–(70) must be satisfied for all possible values of r and s. The indicated summations are performed with j and k varying according to the number of basis functions in each field representation. Equations (67)–(70) hold for $n = 1, 2, 3, \ldots$. The particular value of n determines the azimuthal symmetry of the solution.

Recall the complex amplification factor $\sigma = \sigma_r + i\sigma_i$ introduced in Section 3.1. A marginal state is one for which $\sigma_r = 0$. A stationary instability is one for which $\sigma_i = 0$, and an oscillatory instability is one for which $\sigma_i \neq 0$. Here the mathematical framework needed to study both types of instabilities will be formulated; while it is well known that oscillatory instabilities do not occur in the classical Bénard problem for this geometry,[46] such instabilities are possible when the Soret effect is introduced.[47] Nonetheless, oscillatory instabilities are not the focus of Part I of this study. Herein, the critical value of the Rayleigh number is defined to be the lowest value of the Rayleigh number for the occurrence of a marginal instability in the system, i.e. the minimum value of $\tilde{Ra}_n$ over all n, where $\tilde{Ra}_n$ is the minimum eigenvalue of the solution for each n over all j and k. Physically, the moment any perturbation can convert a sufficient amount of potential energy into kinetic energy to overcome the viscous forces and the stabilizing influence of conduction, the system will become unstable and, according to linear stability theory, a convective flow will ensue.

The pressure can now be eliminated from equation (64) by using the solenoidal property of the velocity basis functions $\mathbf{O}_{jk0}$ coupled with the no-slip boundary condition. Using the divergence theorem,

$$\int_V \mathbf{O}_{rs0}\cdot\nabla P_{jk0}\,\mathrm{d}V = \int_{\partial V} P_{jk0}\mathbf{n}\cdot\mathbf{O}_{rs0}\,\mathrm{d}(\partial V) - \int_V P_{jk0}(\nabla\cdot\mathbf{O}_{rs0})\,\mathrm{d}V, \tag{71}$$

where ∂V denotes the boundary of V, i.e. the walls of the cylinder. Thus, since $\nabla\cdot\mathbf{O}_{rs0} = 0$ and $\mathbf{O}_{rs0}$ vanishes on ∂V, it follows that

$$\int_V \mathbf{O}_{rs0}\cdot\nabla P_{jk0}\,\mathrm{d}V = 0, \tag{72}$$

and the final form of equation (64) is

$$\sum_{j,k}\{-\sigma\langle \mathbf{O}_{rs0}, \mathbf{U}_{jk0}\rangle + \langle \mathbf{O}_{rs0}, \nabla^2 \mathbf{U}_{jk0}\rangle + \langle \mathbf{O}_{rs0}, (\Theta_{jk0}\mathbf{e}_z)\rangle - \psi\langle \mathbf{O}_{rs0}, (\Gamma_{jk0}\mathbf{e}_z)\rangle\} = 0. \tag{73}$$

Equations (67) and (68) can be treated analogously since $\mathbf{V}_{jkn}$ and $\mathbf{W}_{jkn}$ are also solenoidal and vanish on ∂V.

Employing the series representations given in equations (41)–(43) with the basis functions specified in equations (48)–(55) and (60)–63), equations (65), (66) and (73) for the axisymmetric case can be recast into the following forms respectively:

$$\sum_{j,k}\{-(\sigma m_{rjsk} + a_{rjsk})A_{jk} + e_{rjsk}B_{jk} - \psi h_{rjsk}C_{jk}\} = 0, \tag{74}$$

$$\sum_{j,k}\{-(\sigma\widetilde{Pr}n_{rjsk}+g_{rjsk})B_{jk}+\zeta p_{rjsk}C_{jk}+R\widetilde{a}_0(e_{jrks}A_{jk})\}=0, \tag{75}$$

$$\sum\{-q_{rjsk}B_{jk}-(\sigma\widetilde{Sc}o_{rjsk}+y_{rjsk})C_{jk}\}=0. \tag{76}$$

Similarly, for the non-axisymmetric case, employing the series representations given in equations (40), (42) and (43) with the basis functions specified in equations (52)–(63), equations (67)–(70) can be recast into the following forms respectively:

$$\sum_{j,k}\{-(\sigma m_{rjsk}+a_{rjsk})A_{jk}-(\sigma l_{rjsk}+b_{rjsk})D_{jk}+e_{rjsk}B_{jk}-\psi h_{rjsk}C_{jk}\}=0, \tag{77}$$

$$\sum_{j,k}\{-(\sigma x_{rjsk}+c_{rjsk})A_{jk}-(\sigma z_{rjsk}+d_{rjsk})D_{jk}\}=0, \tag{78}$$

$$\sum_{j,k}\{-(\sigma\widetilde{Pr}n_{rjsk}+g_{rjsk})B_{jk}+\zeta p_{rjsk}C_{jk}+R\widetilde{a}_n e_{jrks}A_{jk}\}=0, \tag{79}$$

$$\sum_{j,k}\{-q_{rjsk}B_{jk}-(\sigma\widetilde{Sc}o_{rjsk}+y_{rjsk})C_{jk}\}=0. \tag{80}$$

Here again r and s represent specific values of j and k respectively. For convenience, the subscripts denoting the specific mode have been dropped. These equations must hold for all possible values of r and s. The A_{jk}, D_{jk}, B_{jk} and C_{jk} are the unknown coefficients in the field representations given by equations (41)–(43) or equations (40), (42) and (43); the A_{jk} and D_{jk} belong to the velocity representation, and the B_{jk} and C_{jk} belong to the temperature and η representations respectively. The lower-case letters (a_{rjsk}, b_{rjsk}, etc.) are known coefficients resulting from evaluation of the integrals in equations (65), (66) and (73) or equations (67)–(70), either exactly or using a numerical quadrature with error control.

3.3. The matrix eigenvalue problem

It is convenient to recast the system of equations (74)–(76) (77)–(80) in matrix form. To effect this matrix representation, each set of coefficients A_{jk}, D_{jk}, B_{jk} and C_{jk} is defined as a vector; for example,

$$\mathbf{A}=[A_{jk}]\equiv\begin{bmatrix}A_{11}\\A_{21}\\A_{31}\\\vdots\\A_{12}\\A_{22}\\\vdots\end{bmatrix}. \tag{81}$$

The (r, s) pairs are then used to denote a second index yielding matrices for the lower-case coefficients, i.e.

$$\mathbf{a}=[a_{rjsk}]=\begin{bmatrix}a_{1111}&a_{1211}&a_{1311}&\cdots&a_{1112}&a_{1212}&\cdots\\a_{2111}&a_{2211}&a_{2311}&\cdots&a_{2112}&a_{2212}&\cdots\\a_{3111}&a_{3211}&a_{3311}&\cdots&a_{3112}&a_{3212}&\cdots\\\vdots&\vdots&\vdots&&\vdots&\vdots&\\a_{1121}&a_{1221}&a_{1321}&\cdots&&&\\a_{2121}&a_{2221}&a_{2321}&\cdots&&&\\\vdots&\vdots&\vdots&&&&\end{bmatrix}, \tag{82}$$

and similarly for the other arrays appearing in equations (74)–(76) or (77)–(80). The matrix forms of equations (74)–(76) are respectively

$$(\sigma\mathbf{m}+\mathbf{a})\mathbf{A}=\mathbf{eB}-\psi\mathbf{hC}, \tag{83}$$

$$(\sigma\tilde{Pr}\mathbf{n}+\mathbf{g})\mathbf{B}=\tilde{Ra}_0\mathbf{e}^{\mathrm{T}}\mathbf{A}+\zeta\mathbf{pC}, \tag{84}$$

$$(\sigma\tilde{Sc}\mathbf{o}+\mathbf{y})\mathbf{C}=-\mathbf{qB}, \tag{85}$$

where a superscript T denotes a transpose. For the non-axisymmetric case, the matrix forms of equations (77)–(80) respectively

$$(\sigma\mathbf{m}+\mathbf{a})\mathbf{A}+(\sigma\mathbf{l}+\mathbf{b})\mathbf{D}=\mathbf{eB}-\psi\mathbf{hC}, \tag{86}$$

$$(\sigma\mathbf{x}+\mathbf{c})\mathbf{A}+(\sigma\mathbf{z}+\mathbf{d})\mathbf{D}=0, \tag{87}$$

$$(\sigma\tilde{Pr}\mathbf{n}+\mathbf{g})\mathbf{B}=\zeta\mathbf{pC}+\tilde{Ra}_n\mathbf{e}^{\mathrm{T}}\mathbf{A}, \tag{88}$$

$$(\sigma\tilde{Sc}\mathbf{o}+\mathbf{y})\mathbf{C}=-\mathbf{qB}. \tag{89}$$

The second momentum equation has an abbreviated form because $\mathbf{W}_{jkn}$ has no vertical component, a property which also accounts for the lack of a companion term to $\mathbf{e}^{\mathrm{T}}\mathbf{A}$ in the energy equation.

Considering the marginal oscillatory state, in which $\sigma_r = 0$ but $\sigma_i \neq 0$, it is convenient to recast equations (83)–(85) into the following partitioned matrix eigenvalue problem for the axisymmetric case:

$$\begin{bmatrix} -\mathbf{a} & \mathbf{e} & -\psi\mathbf{h} \\ \tilde{Ra}_0\mathbf{e}^{\mathrm{T}} & -\mathbf{g} & \zeta\mathbf{p} \\ 0 & -\mathbf{q} & -\mathbf{y} \end{bmatrix}\begin{bmatrix}\mathbf{A}\\ \mathbf{B}\\ \mathbf{C}\end{bmatrix}=\sigma\begin{bmatrix}\mathbf{m} & 0 & 0\\ 0 & \tilde{Pr}\mathbf{n} & 0\\ 0 & 0 & \tilde{Sc}\mathbf{o}\end{bmatrix}\begin{bmatrix}\mathbf{A}\\ \mathbf{B}\\ \mathbf{C}\end{bmatrix} \tag{90}$$

or

$$\mathbf{Lx}=\sigma\mathbf{Mx}, \tag{91}$$

which is the standard form for a general eigenvalue problem. Analogously, for the non-axisymmetric case it is convenient to recast equations (86)–(89) into the corresponding partitioned matrix form:

$$\begin{bmatrix} -\mathbf{a} & -\mathbf{b} & \mathbf{e} & -\psi\mathbf{h} \\ -\mathbf{c} & -\mathbf{d} & 0 & 0 \\ \tilde{Ra}_n\mathbf{e}^{\mathrm{T}} & 0 & -\mathbf{g} & \zeta\mathbf{p} \\ 0 & 0 & -\mathbf{q} & -\mathbf{y} \end{bmatrix}\begin{bmatrix}\mathbf{A}\\ \mathbf{D}\\ \mathbf{B}\\ \mathbf{C}\end{bmatrix}=\sigma\begin{bmatrix}\mathbf{m} & \mathbf{l} & 0 & 0\\ \mathbf{x} & \mathbf{z} & 0 & 0\\ 0 & 0 & \tilde{Pr}\mathbf{n} & 0\\ 0 & 0 & 0 & \tilde{Sc}\mathbf{o}\end{bmatrix}\begin{bmatrix}\mathbf{A}\\ \mathbf{D}\\ \mathbf{B}\\ \mathbf{C}\end{bmatrix} \tag{92}$$

or

$$\mathbf{Lx}=\sigma\mathbf{Mx}, \tag{93}$$

with **L**, **M** and **x** redefined appropriately as implied. The marginal stability problem then becomes one of finding those parameter space configurations, i.e. configurations of $(\tilde{Ra}, \psi, \zeta, \tilde{Pr}, \tilde{Sc}, \sigma_i)$, for which simultaneously $\sigma_r = 0$ and $\tilde{Ra}$ is the minimum of $\tilde{Ra}_n$ over all n for a specified value of gamma. This search requires an iteration process in order to determine the marginally stable surfaces in the six-dimensional parameter space. The special case of a marginal stationary disturbance, i.e. $\sigma_i = 0$, can be simplified. For the axisymmetric case, equation (85) is solved for **C** and equation (83) for **A**, and these are substituted into equation (84) to obtain a smaller

eigenvalue problem explicitly for $\widetilde{Ra}_0$:

$$\{(\mathbf{g}+\zeta\mathbf{p}\mathbf{y}^{-1}\mathbf{q})^{-1}\mathbf{e}^{\mathrm{T}}\mathbf{a}^{-1}(\mathbf{e}+\psi\mathbf{h}\mathbf{y}^{-1}\mathbf{q})\}\mathbf{B}=\left(\frac{1}{\widetilde{Ra}_0}\right)\mathbf{B}. \tag{94}$$

Analogously for the non-axisymmetric case, equation (87) is solved for **D** and equation (89) for **C**, and these are substituted into equation (86), which is solved for **A** to yield

$$\mathbf{A}=(\mathbf{a}-\mathbf{b}\mathbf{d}^{-1}\mathbf{c})^{-1}(\mathbf{e}+\psi\mathbf{h}\mathbf{y}^{-1}\mathbf{q})\mathbf{B}. \tag{95}$$

This is then substituted into equation (88) to yield

$$\{(\mathbf{g}+\zeta\mathbf{p}\mathbf{y}^{-1}\mathbf{q})^{-1}\mathbf{e}^{\mathrm{T}}(\mathbf{a}-\mathbf{b}\mathbf{d}^{-1}\mathbf{c})^{-1}(\mathbf{e}+\psi\mathbf{h}\mathbf{y}^{-1}\mathbf{q})\}\mathbf{B}=\left(\frac{1}{\widetilde{Ra}_n}\right)\mathbf{B}. \tag{96}$$

In either case, the solution then yields the minimal value of $\widetilde{Ra}_n$, i.e. the critical value for mode n, directly. The minimum value of $\widetilde{Ra}_n$ over all n is the critical Rayleigh number for the onset of convection.

Before proceeding to the actual solution of equation (90) or (94) and equation (92) or (96), it is useful to investigate the limiting case of a pure (i.e. monocomponent) fluid system. For the axisymmetric case it is easily verified that, as expected, if the values of the new physical parameters ψ and ζ are set to zero along with σ_i, the eigenvalue problem for the pure fluid system studied by Charlson and Sani[41] is regenerated. For $\psi=0$ and $\zeta=0$, equation (94) simplifies to

$$\{\mathbf{g}^{-1}\mathbf{e}^{\mathrm{T}}\mathbf{a}^{-1}\mathbf{e}\}\mathbf{B}=\left(\frac{1}{\widetilde{Ra}_0}\right)\mathbf{B}. \tag{97}$$

As shown there, since **g** is a diagonal matrix and **a** is symmetric, the substitution $\tilde{\mathbf{B}}=\mathbf{g}^{1/2}\mathbf{B}$ leads to a symmetric eigenvalue problem which simplifies the numerical computation. Similarly, performing an analogous manipulation for the non-axisymmetric case, the eigenvalue problem for the pure fluid system studied by Buell and Catton[44] is regenerated. It is noteworthy that for $\psi=0$ and $\zeta=0$, equation (96) simplifies to

$$\{(\mathbf{g}^{-1}\mathbf{e}^{\mathrm{T}}(\mathbf{a}-\mathbf{b}\mathbf{d}^{-1}\mathbf{c})^{-1}\mathbf{e})\}\mathbf{B}=\left(\frac{1}{\widetilde{Ra}_n}\right)\mathbf{B}, \tag{98}$$

which can be transformed to a symmetric form. Substituting for B from equation (95), equation (98) can be rewritten to yield the matrix eigenvalue problem solved by Buell and Catton. For the binary case the eigenvalue problem is no longer symmetric, and there are the additional parameters $\widetilde{Sc}$, ψ, and ζ.

The solution of the eigenvalue problem was generated numerically. The numbers of basis functions used in the approximate solutions given by equations (40)–(43) are as follows: for axisymmetric solutions, ten radial and four vertical functions were used for each field, resulting in a 40-term series for each field for each mode; for non-axisymmetric solutions, ten radial and six vertical functions were used, resulting in a 120-term series for the velocity field and a 60-term series for Θ and Γ for each mode. These specifications resulted in estimated relative errors in the computed Rayleigh numbers of order 10^{-3} or less for binary fluid mixtures, and of order 10^{-4} for monocomponent fluids. These estimates were made by varying the number of basis functions in order to study the convergence of the series representation of the field variables. This was supplemented in the monocomponent case by lower-bound estimates due to Charlson and Sani.[43] Unfortunately, in the case of eigenvectors, no quantitative error estimates could be obtained, but comparison with recent independent numerical simulations suggests that the

eigenvectors are also accurate. In all cases considered it was found that the critical Rayleigh numbers for the 'odd' solutions for a given mode (n) were significantly larger than those for the 'even' solutions. Consequently, for all of the linear stability results which follow it is implied that $\tilde{Ra}_n$ is the minimum eigenvalue of the matrix problem for the even solution for that mode n. This appears to agree with observation, i.e. convection always sets in with one recirculation cell in the vertical, regardless of the cylinder aspect ratio.

4. LINEAR STABILITY RESULTS

4.1. A comparison with experiments and other theories

A primary purpose of this work is to explore how varying the concentration of a binary mixture affects the onset of convection. As discussed previously, the addition of a second component introduces the Soret and Dufour effects as additional driving forces for mass and heat transfer respectivley, thus affecting the stability of the mixture. Abernathey and Rosenberger[28] experimentally observed the onset of convection in mixtures of xenon and helium (Xe–He) and xenon and argon (Xe–Ar) at various concentrations in a vertical right circular cylinder with highly conducting, thick copper walls. The aspect ratio of the cylinder was $\gamma = 1/6$, and it was heated from below. Their results are shown in Figures 2 and 3 along with the theoretical values generated in the present study, those of Crespo and Velarde[29] and those of Hardin[33] and Henry.[31] The results from the past two works are virtually identical; both studies used an accurate Galerkin scheme with the same trial functions which were the velocity trial functions used by Charlson and Sani,[43] and essentially the same temperature and concentration (η) trial

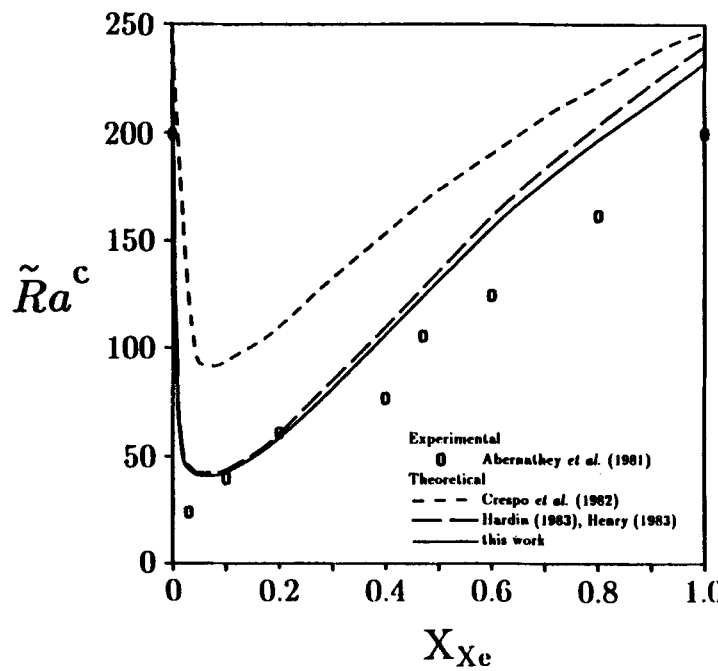

Figure 2. Marginal stability for Xe–He mixtures for $\gamma = 1/6$

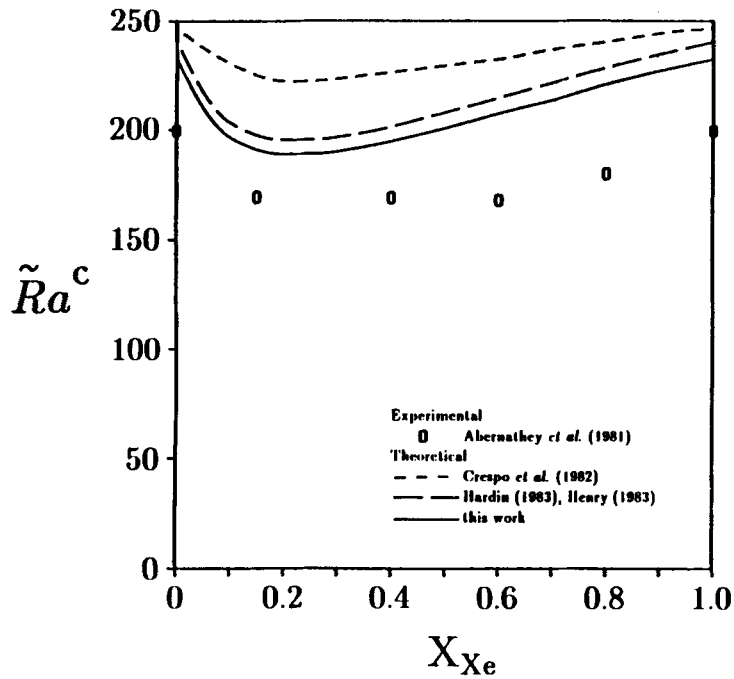

Figure 3. Marginal stability for Xe–Ar mixtures for $\gamma = 1/6$

functions used in the present study. In all cases the critical mode was found to be $n = 1$ with one vertical roll similar to the structure shown in Figure 14 except with one radial roll. These particular fluid pairs were chosen because for them ψ and η can be computed fairly accurately using molecular theory, thus avoiding the difficulty of finding reliable experimental values. Consequently, when comparing the experimental and theoretical results it should be noted that the values of the Soret and Dufour parameters ψ and η used in the numerical computations were *calculated* from collision theory for ideal monoatomic gas mixtures.[28]

The critical Rayleigh numbers computed by Crespo and Velarde using a one-term Galerkin trial function are substantially too high. The probable reason for this is that their one-term trial function is not sufficient to accurately resolve the physics in a small-aspect-ratio cylinder, where sidewall effects are important. The much more accurate multiple-term Galerkin schemes of Hardin[33] and Henry[31] are in very good agreement with, but slightly above, the experimental observations. The results of the present work appear to be slightly better still. (For this problem it is expected that the numerical results will approach the true threshold from above as the approximation is improved. This behaviour has been proven for the monocomponent case.[46]) In contrast, in a physical experiment approximating perfectly conducting walls, any non-idealities in the boundary conditions would lead to a lower critical Rayleigh number since the density gradient would not necessarily be strictly antiparallel to the gravitational vector, which is a necessary condition in order for a hydrostatic base state to exist. Moreover, Buell and Catton[44] showed, at least in the monocomponent case, that as the conductivity of the wall is decreased, the stability threshold is decreased. These effects, coupled with the possibility of geometric imperfections in the experimental apparatus, point to some difficulties in performing the physical experiments, which could be contributing factors to the remaining discrepancies between the

experimental and theoretical results. Abernathey and Rosenberger[28] reported $\mathscr{R}^c = 200 \pm 20$ as the critical Rayleigh number for the onset of convection in a monocomponent fluid, compared to our computed value of $\mathscr{R}^c = 233$; however, the original result reported by Olson and Rosenberger[47] for the monocomponent case was $\mathscr{R}^c = 220 \pm 12$. (Note that for convenience in discussing results for cylinders with small aspect ratios, where the values of $\tilde{Ra}^c$ are very large, an alternative Rayleigh number will be used: $\tilde{\mathscr{R}} \equiv \gamma^4 \tilde{Ra}$.)

It is noteworthy that, in general, the predicted stability limit is larger than the experimental one by more than the estimate of error in the theoretical values. Since the values of physical properties which were used were those utilized by Abernathy and Rosenberger,[28] we believe that the disparity in values is possibly due to experimental problems such as heat loss and/or inclination of the cylinder, which could cause a feeble precursor flow, thus complicating the determination of the point of onset of convection.

4.2. The effect of varying the concentration

The general shapes of the marginal stability curves of $\tilde{\mathscr{R}}^c$ (or $\tilde{Ra}^c$) versus concentration for mixtures of Xe–He and Xe–Ar remain consistent as a function of aspect ratio. Also, although the actual critical Rayleigh numbers are found to be somewhat less for these mixtues contained in a cylinder with an insulating sidewall compared to one with a conducting sidewall, the same general shapes are found for the marginal stability curves. Even the results for a horizontally infinite layer show a similar variation with composition, as can be seen from Figure 4. In this figure the various theoretical curves are all normalized to give the experimental value $\mathscr{R}^c = 200$ at $X_{Xe} = 0$. (Here X_{Xe} represents the volume-averaged mole fraction of xenon in the mixture.) It is noteworthy that

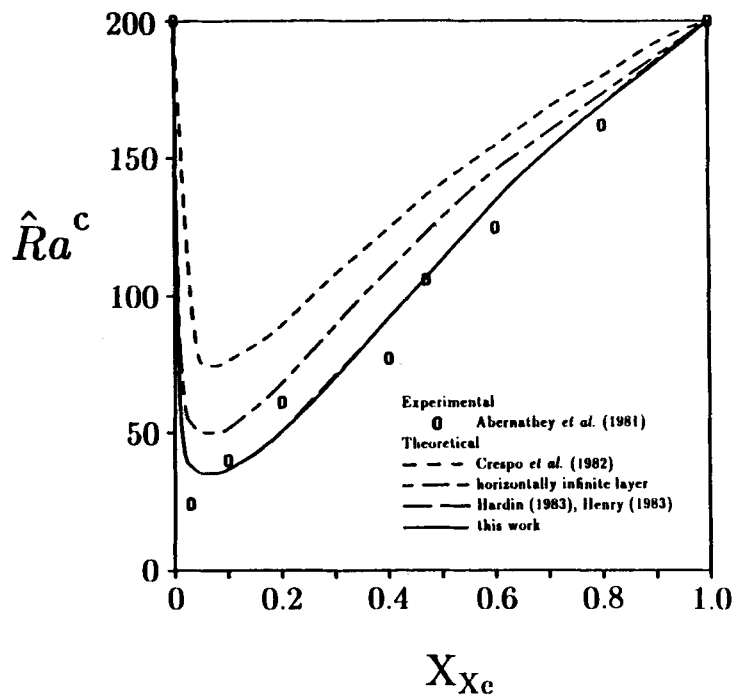

Figure 4. Normalized marginal stability curves for Xe–He for $\gamma = 1/6$

while the results of Crespo and Velarde[29] underestimate the destabilization afforded by the Soret and Dufour effects, the present study appears to agree well with experimental observations.

As the aspect ratio is increased, so that we are considering shorter, fatter cylinders, the stabilizing influence of the sidewall is diminished, so that the entire stability threshold occurs at lower values of $R\tilde{a}^c$. This feature is illustrated in Tables I and II, where the critical Rayleigh number is listed at a series of aspect ratios for a monocomponent system, an Xe–He mixture with

Table I. Critical Rayleigh number as a function of aspect ratio for a conducting sidewall

	$R\tilde{a}^c$					
γ	Monocomponent		Xe–Ar ($X_{Xe} = 0{\cdot}2$)		Xe–He ($X_{Xe} = 0{\cdot}05$)	
0·05	$3{\cdot}471 \times 10^7$	(1, 1)	$2{\cdot}929 \times 10^7$	(1, 1)	8.975×10^6	(1, 1)
0·1	2.213×10^6	(1, 1)	$1{\cdot}872 \times 10^6$	(1, 1)	$5{\cdot}777 \times 10^5$	(1, 1)
1/6	$3{\cdot}020 \times 10^5$	(1, 1)	$2{\cdot}563 \times 10^5$	(1, 1)	$8{\cdot}018 \times 10^4$	(1, 1)
0·3	$3{\cdot}525 \times 10^4$	(1, 1)	$3{\cdot}013 \times 10^4$	(1, 1)	9659	(1, 1)
0·4	$1{\cdot}427 \times 10^4$	(1, 1)	$1{\cdot}224 \times 10^4$	(1, 1)	3956	(1, 1)
0·5	8012	(1, 1)	6888	(1, 1)	2228	(1, 1)
0·75	3972	(1, 1)*	3452	(1, 1)	1111	(1, 1)
1	2545	(0, 2)	2330	(0, 2)	872·5	(1, 1)
1·5	2010	(0, 2)	1809	(0, 2)	729·3	(0, 2)
2	1883	(1, 3)	1703	(1, 3)	674·6	(0, 2)
2·5	1810	(0, 4)	1642	(0, 5)	666·8	(0, 2)*
3	1783	(0, 6)	1620	(1, 5)	659·7	(0, 4)
3·5	1759	(0, 6)	1598	(0, 6)	653·2	(0, 4)
4	1749	(0, 8)	1591	(0, 8)	651·5	(0, 4)

* A new roll has begun to grow but its extent is so small it has not been counted.

Table II. Critical Rayleigh number as a function of aspect ratio for an insulating sidewall

	$R\tilde{a}^c$					
γ	Monocomponent		Xe–Ar ($X_{Xe} = 0{\cdot}2$)		Xe–He ($X_{Xe} = 0{\cdot}05$)	
0·05	$1{\cdot}101 \times 10^7$	(1, 1)	$1{\cdot}035 \times 10^7$	(1, 1)	5.661×10^6	(1, 1)
0·1	7.135×10^5	(1, 1)	$6{\cdot}702 \times 10^5$	(1, 1)	$3{\cdot}662 \times 10^5$	(1, 1)
1/6	$1{\cdot}010 \times 10^5$	(1, 1)	$9{\cdot}479 \times 10^4$	(1, 1)	$5{\cdot}149 \times 10^4$	(1, 1)
0·3	$1{\cdot}321 \times 10^4$	(1, 1)	$1{\cdot}235 \times 10^4$	(1, 1)	6506	(1, 1)
0·4	5964	(1, 1)	5540	(1, 1)	2798	(1, 1)
0·5	3774	(1, 1)	3476	(1, 1)	1661	(1, 1)
0·75	2592	(1, 1)	2317	(1, 1)	931·8	(1, 1)
1	2260	(0, 2)	2086	(0, 2)	793·9	(1, 1)
1·5	1895	(0, 2)	1703	(0, 2)	701·0	(0, 2)
2	1832	(1, 3)	1655	(1, 3)	662·6	(0, 2)
2·5	1781	(0, 4)	1613	(0, 4)	660·6	(1, 3)
3	1768	(1, 5)	1604	(1, 5)	656·5	(0, 4)
3·5	1747	(0, 6)	1587	(0, 6)	650·5	(0, 4)
4	1746	(1, 7)	1588	(1, 7)	651·6	(0, 4)

a xenon mole fraction of $X_{Xe} = 0{\cdot}05$, and an Xe–Ar mixture with a xenon mole fraction of $X_{Xe} = 0{\cdot}2$, for a cylinder with a conducting or insulating sidewall. These xenon mole fractions represent the mole fractions at which ψ is approximately a maximum for these fluid pairs.

The integers in parentheses in Tables I–IV characterize the spatial structure of the critical mode: the first integer characterizes the azimuthal roll structure while the second characterizes the radial structure. Specifically, the 'radial' structure is given as the number of closed rolls counted across the diameter on a vertical plane through the centre of the cylinder. For an axisymmetric flow, 'two rolls' correspond to one toroidal roll cell. In all cases the vertical structure is unicellualr.

The convective destabilization afforded by the Soret effect is much greater for the Xe–He system than for the Xe–Ar system. This is to be expected because of the much greater molecular weight difference between the two constituents in the Xe–He system.[28] Xenon has a positive thermal diffusion coefficient (D') in both systems. Consequently, xenon preferentially moves toward the top, i.e. the cold end, in these systems. Since xenon is the heavier species of both fluid pairs, this migration reinforces the unstable density stratification resulting from the imposed temperature gradient. However, since the molecular weight ratio is 32·8 for the Xe–He system compared to 3·28 for the Xe–Ar system, the relative density stratification due to the Soret effect will be correspondingly greater for the Xe–He system.

4.3. The contribution from the Dufour effect

The convective destabilization afforded by the Dufour effect can also be much greater for the Xe–He system than for the Xe–Ar system, which illustrates the coupling of the Soret and Dufour effects according to the thermodynamics of irreversible processes, as expressed in the Onsager reciprocal relations.[4] (Recall that the Soret effect is also called thermal diffusion, while the Dufour effect is also called the diffusion-thermo effect.) Corresponding to their difference in molecular weight ratios, the magnitudes of both ψ and ζ, the dimensionless Soret and Dufour parameters, are an order of magnitude greater for the Xe–He system than for the Xe–Ar system. However, while the relatively greater destabilization due to the Dufour effect in the Xe–He system generally parallels the relatively greater Soret contribution in this system, for both systems the Dufour effect is seen from Tables III and IV to play only a minor role compared to the Soret effect,

Table III. A comparison of critical Rayleigh numbers calculated with and without the Dufour effect contribution; Xe–He system; conducting sidewall

	$\widetilde{Ra}^c$					
	$\gamma = 1/6$		$\gamma = 1$		$\gamma = 4$*	
X_{Xe}	With	Without	With	Without	With	Without
0	$3{\cdot}020 \times 10^5$ (1, 1)	$3{\cdot}020 \times 10^5$ (1, 1)	2545 (0, 2)	2545 (0, 2)	1749 (0, 8)	1749 (0, 8)
0·01	$1{\cdot}133 \times 10^5$ (1, 1)	$1{\cdot}134 \times 10^5$ (1, 1)	1243 (1, 1)	1244 (1, 1)	885·9 (0, 6)	888·0 (0, 6)
0·025	$8{\cdot}298 \times 10^4$ (1, 1)	$8{\cdot}303 \times 10^4$ (1, 1)	903·7 (1, 1)	903·6 (1, 1)	673·2 (0, 4)	674·6 (0, 4)
0·05	$8{\cdot}018 \times 10^4$ (1, 1)	$8{\cdot}015 \times 10^4$ (1, 1)	872·5 (1, 1)	871·3 (1, 1)	651·5 (0, 4)	652·5 (0, 4)
0·1	$8{\cdot}703 \times 10^4$ (1, 1)	$8{\cdot}690 \times 10^4$ (1, 1)	950·0 (1, 1)	947·2 (1, 1)	701·0 (0, 4)	703·6 (0, 4)
0·2	$1{\cdot}138 \times 10^5$ (1, 1)	$1{\cdot}140 \times 10^5$ (1, 1)	1249 (1, 1)	1250 (1, 1)	880·4 (0, 6)	891·3 (0, 6)
0·4	$1{\cdot}836 \times 10^5$ (1, 1)	$1{\cdot}858 \times 10^5$ (1, 1)	1886 (0, 2)	1938 (0, 2)	1264 (0, 8)	1295 (0, 8)
0·6	$2{\cdot}441 \times 10^5$ (1, 1)	$2{\cdot}483 \times 10^5$ (1, 1)	2240 (0, 2)	2294 (0, 2)	1528 (0, 8)	1563 (0, 8)
0·8	$2{\cdot}834 \times 10^5$ (1, 1)	$2{\cdot}867 \times 10^5$ (1, 1)	2445 (0, 2)	2478 (0, 2)	1678 (0, 8)	1700 (0, 8)

* In the $\gamma = 4$ case the spatial structure assessment is less precise because of the larger number of radial rolls.

Table IV. A comparison of critical Rayleigh numbers calculated with and without the Dufour effect contribution; Xe–Ar system; conducting sidewall

	$\widetilde{Ra}^c$					
	$\gamma = 1/6$		$\gamma = 1$		$\gamma = 4$*	
X_{Xe}	With	Without	With	Without	With	Without
0	$3{\cdot}020 \times 10^5$ (1, 1)	$3{\cdot}020 \times 10^5$ (1, 1)	2545 (0, 2)	2545 (0, 2)	1749 (0, 8)	1749 (0, 8)
0·1	$2{\cdot}633 \times 10^5$ (1, 1)	$2{\cdot}639 \times 10^5$ (1, 1)	2366 (0, 2)	2371 (0, 2)	1617 (0, 8)	1620 (0, 8)
0·2	$2{\cdot}563 \times 10^5$ (1, 1)	$2{\cdot}572 \times 10^5$ (1, 1)	2330 (0, 2)	2338 (0, 2)	1591 (0, 8)	1596 (0, 8)
0·3	$2{\cdot}585 \times 10^5$ (1, 1)	$2{\cdot}594 \times 10^5$ (1, 1)	2340 (0, 2)	2350 (0, 2)	1598 (0, 8)	1605 (0, 8)
0·4	$2{\cdot}643 \times 10^5$ (1, 1)	$2{\cdot}652 \times 10^5$ (1, 1)	2368 (0, 2)	2378 (0, 2)	1619 (0, 8)	1626 (0, 8)
0·6	$2{\cdot}786 \times 10^5$ (1, 1)	$2{\cdot}794 \times 10^5$ (1, 1)	2437 (0, 2)	2444 (0, 2)	1670 (0, 8)	1675 (0, 8)
0·8	$2{\cdot}919 \times 10^5$ (1, 1)	$2{\cdot}924 \times 10^5$ (1, 1)	2498 (0, 2)	2503 (0, 2)	1716 (0, 8)	1719 (0, 8)

* In the $\gamma = 4$ case the spatial structure assessment is less precise because of the larger number of radial rolls.

resulting in a maximum destabilization of about 3% for the Xe–He system and about 0·5% for the Xe–Ar system. The relatively minor importance of the Dufour effect in these fluid systems is in apparent agreement with Crespo and Velarde,[29] but is somewhat contrary to the expectations of Ybarra and Velarde[25] and Gutkowicz-Krusin *et al.*,[26,27] who suggested that the Dufour effect should be important in gaseous systems, where κ/D is approximately unity, such that the Soret and Dufour effects operate on comparable time scales.

There is one surprising feature of Table III. For the Xe–He system at xenon mole fractions of $0{\cdot}01 < X_{Xe} < 0{\cdot}2$ for $\gamma = 1/6$ and $\gamma = 1$, the Dufour effect is *stabilizing*. In these cases the flow is antisymmetric ($n = 1$); this was not observed in this concentration range at $\gamma = 4$ where the flow is axisymmetric. Also, isolated results suggest that this only occurs when the cylinder sidewall is conducting. Evidently this slight stabilization is the result of some subtle interaction between the fluid and a conducting sidewall. It does not appear to be a numerical artefact, since the relative errors in the numbers in Table III are of order 10^{-4} for the number of trial functions used to generate these results. In any case, this effect seems rather insignificant, resulting in a maximum stabilization of about 0·5%. In view of its relatively minor role, the contribution of the Dufour effect is neglected in the remainder of the calculations presented, unless a specific fluid system (i.e. an Xe–He or Xe–Ar mixture) is being described. The primary reason for this is to reduce the dimension of the parameter space by one.

4.4. The effects of changing the cylinder aspect ratio

4.4.1. General results for monocomponent fluids. A closer inspection of Tables I and II shows that for small aspect ratios, the percentage decrease in $\widetilde{Ra}^c$ resulting from the Soret effect is larger for the case of cylinder with a conducting sidewall than for one with an insulating sidewall. This effect will be discussed more thoroughly for general systems in a subsequent paper.

While the general trend is for $\widetilde{Ra}^c$ to decrease as γ increases, as seen from Tables I and II, the dependence of $\widetilde{Ra}^c$ on γ is not a simple one. This is illustrated in several figures. Figures 5 and 6 show the stability limits of the first four modes for a monocomponent fluid in a cylinder with a conducting or insulating sidewall respectively at aspect ratios $\gamma \leq 1{\cdot}5$. Figures 7 and 8 show the stability limits of the first four modes for an Xe–He mixture with a xenon mole fraction of $X_{Xe} = 0{\cdot}05$ for a cylinder with a conducting or insulating sidewall respectively at aspect ratios $\gamma \leq 1{\cdot}5$.

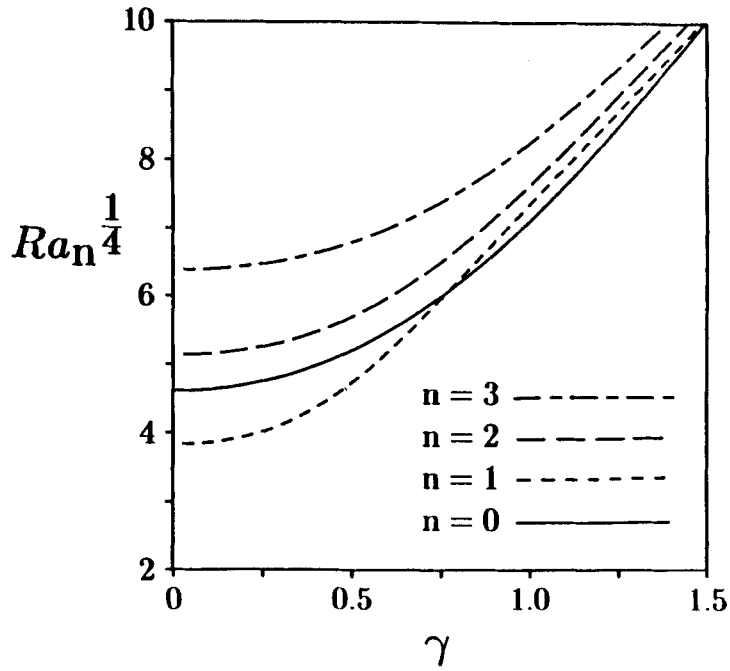

Figure 5. Modal stability curves for a monocomponent fluid for $\gamma \leq 1{\cdot}5$ with a conducting sidewall

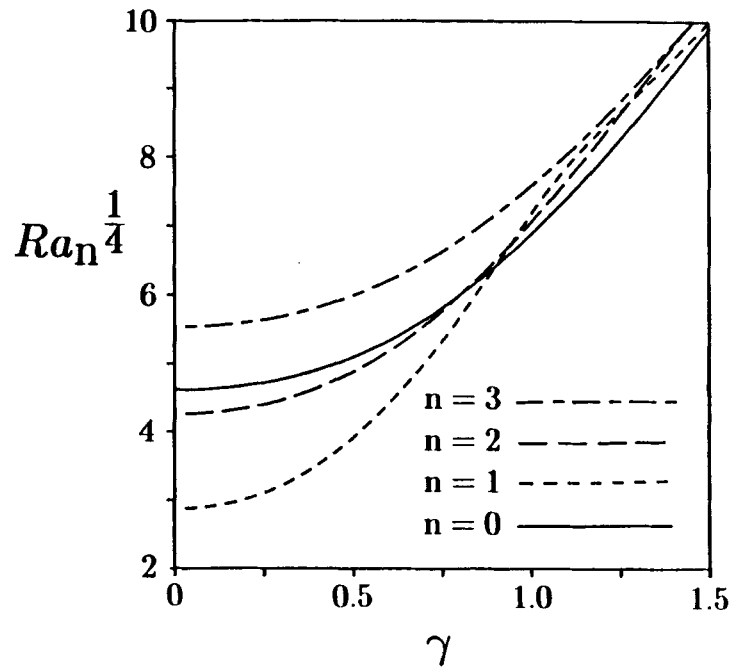

Figure 6. Modal stability curves for a monocomponent fluid for $\gamma \leq 1{\cdot}5$ with an insulating sidewall

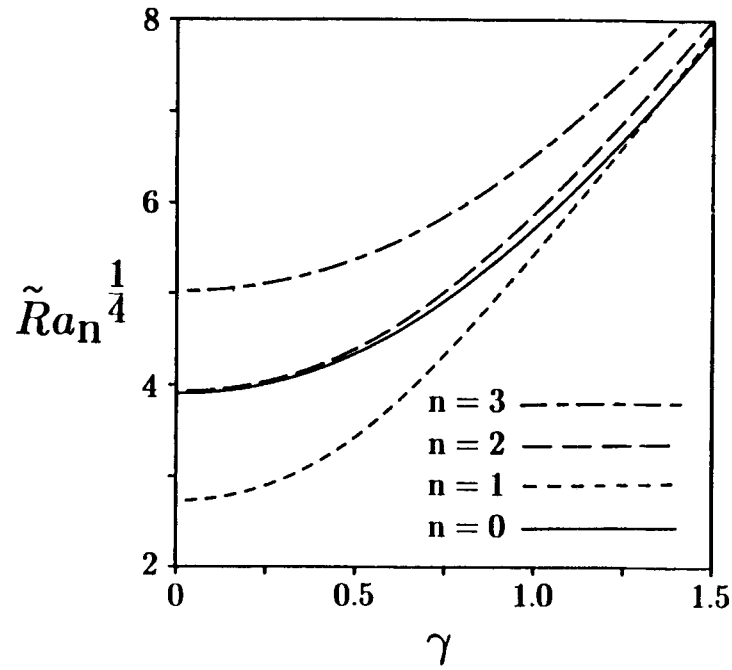

Figure 7. Modal stability curves for Xe–He, $X_{Xe} = 0{\cdot}05$, for $\gamma \leq 1{\cdot}5$ with a conducting sidewall

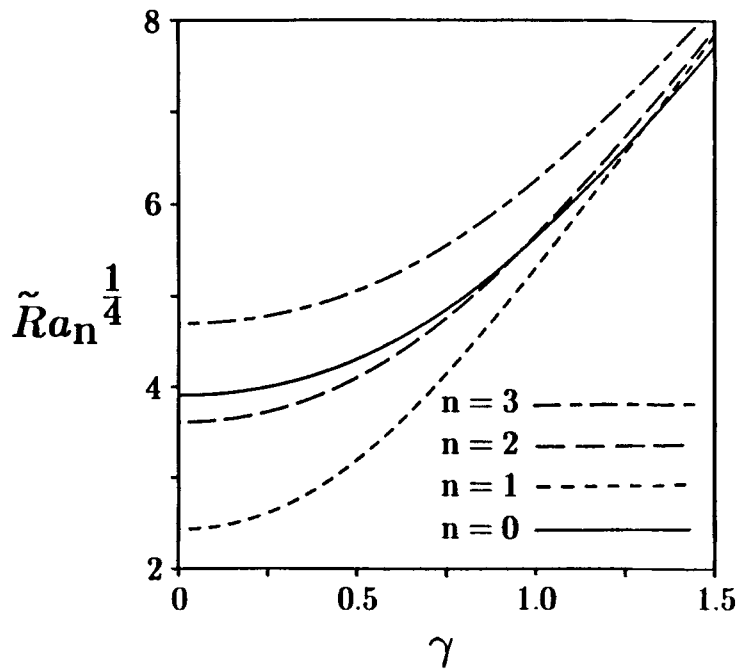

Figure 8. Modal stability curves for Xe–He, $X_{Xe} = 0{\cdot}05$, for $\gamma \leq 1{\cdot}5$ with an insulating sidewall

These figures display the critical Rayleigh number for the least stable mode as a function of aspect ratio; the critical mode, and consequently the spatial structure of the incipient flow, varies over this interval in each figure. In this range of aspect ratios, essentially a single antisymmetric ($n = 1$) roll fills the cylinder for the lower end of the range, while a single axisymmetric ($n = 0$) toroidal roll fills the cylinder at the upper end. The aspect ratio at which the transition between the two modes occurs depends on the specific fluid mixture and the boundary conditions. More information on this provided in Tables I–IV.

Figures 9, 10, 11 and 12 respectivley show the stability limits for the first four modes for the same four cases as Figures 5, 6, 7 and 8 but for aspect ratios $1 \leq \gamma \leq 4$. Over this interval the critical mode and the corresponding flow structure vary in a complicated fashion, with several transitions in the critical mode and corresponding flow structure. For a cylinder with an insulating sidewall it can be seen from Figures 10 and 12 that the decrease in $\tilde{Ra}^c$ with γ is not even monotonic. Here again the spatial structure varies along each curve in the figures as indicated in Tables I–IV. The situation is further complicated by the rather complex interplay between the $\tilde{Ra}_n$ for the various modes as a function of γ, different modes assuming the role of the critical mode over different intervals of γ depending on the particular fluid system. This implies that the flow structure at the onset of convection is highly dependent on γ over the range of γ shown. The most important roles are played by the $n = 0$ and $n = 1$ modes. The stability curves for these two modes as a function of γ are seen to cross periodically, and usually one or the other of these modes is the critical mode. These features have not been previously explained, even for the monocomponent case, although for a cylinder with an insulating sidewall Charlson and Sani[43] noted the approximate concurrence of a change in the critical mode with a change in the number of rolls for the axisymmetric mode. Buell and Catton[44] noted the rich behaviour of the

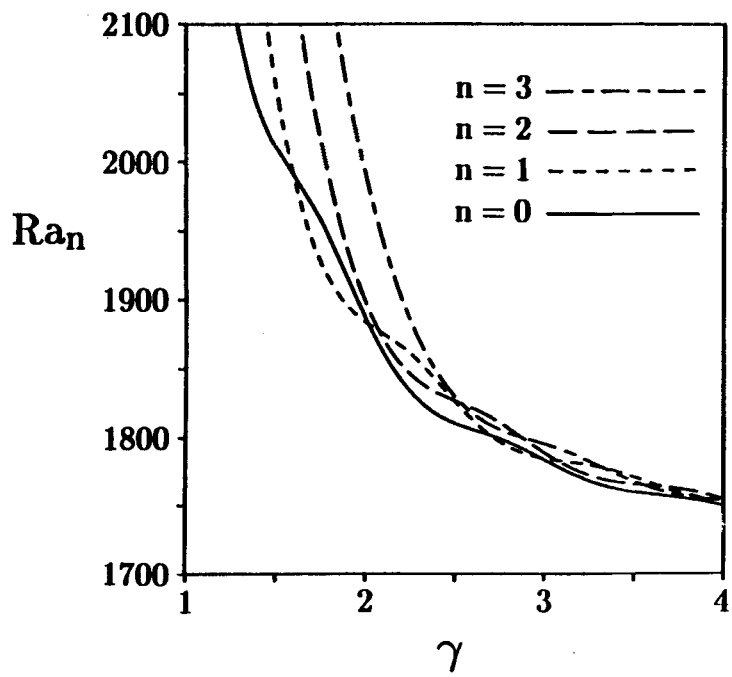

Figure 9. Modal stability curves for a monocomponent fluid for $1 \leq \gamma \leq 4$ with a conducting sidewall

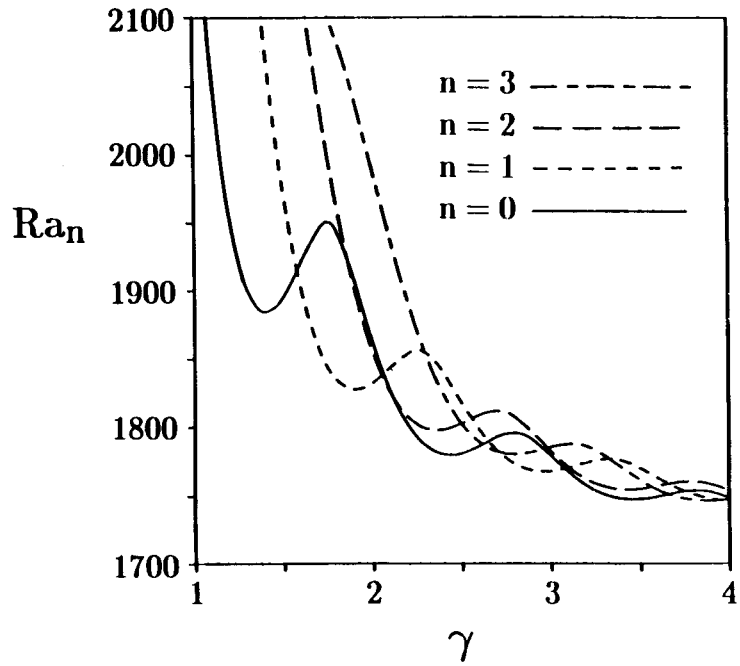

Figure 10. Modal stability curves for a monocomponent fluid for $1 \leq \gamma \leq 4$ with an insulating sidewall

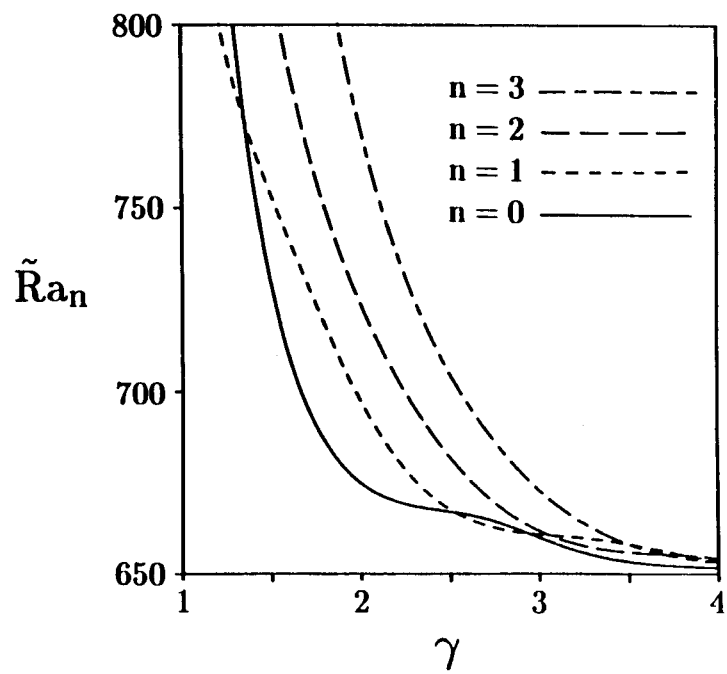

Figure 11. Modal stability curves for Xe–He, $X_{Xe} = 0{\cdot}05$, for $1 \leq \gamma \leq 4$ with an insulating sidewall

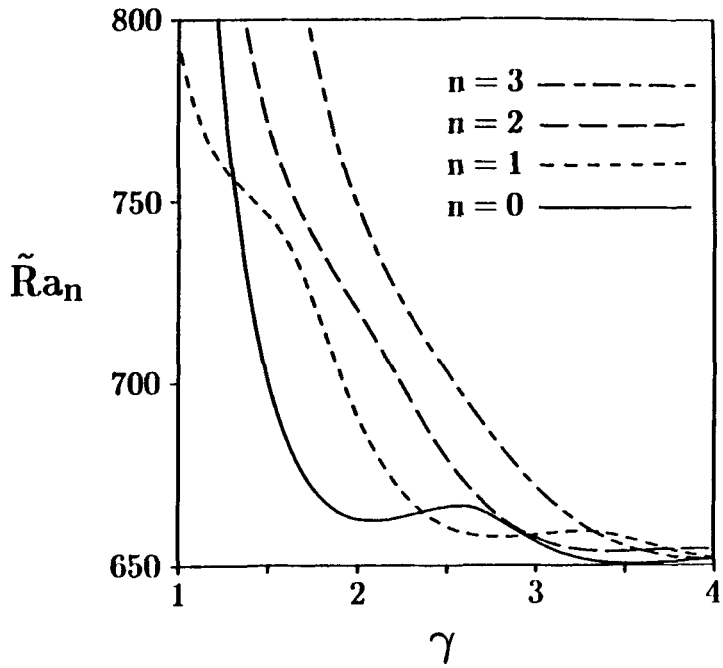

Figure 12. Modal stability curves for Xe–He, $X_{Xe} = 0{\cdot}05$, for $1 \leq \gamma \leq 4$ with an insulating sidewall

monocomponent stability limits but did not discuss them. These particularities allude to some fascinating physics which result from the finite geometry.

In the mathematical model used herein, a variety of recirculation patterns can occur, each with a different azimuthal symmetry corresponding to the value of n, which can be thought of as an azimuthal 'wave number'. For each mode type, specified by its n-value, the number of roll cells for a particular fluid system at the critical $\tilde{Ra}_n$ for that mode is determined by the aspect ratio (γ) and the boundary conditions. Examples of the spatial structures of flows corresponding to the two most commonly critical modes (i.e. the $n = 0$ and $n = 1$ modes) are illustrated in Figures 13 and 14 by 3D perspective vector plots of the velocity field for each of these modes at the onset of convection for an aspect ratio at which it is the critical mode. Figure 13 shows one axisymmetric ($n = 0$) radial roll cell, or two roll recirculations counted across the diameter, in a cylinder with an aspect ratio $\gamma = 1$. Figure 14 shows one-and-a-half antisymmetric ($n = 1$) radial roll cells, or three complete rolls counted across the diameter, in a cylinder with an aspect ratio $\gamma = 1{\cdot}8$. Here *radial* rolls means the number of rolls counted across the cylinder from $r = 0$ to $r = 1$. For the finite geometry, antisymmetric ($n = 1$) solutions correspond to an odd number of roll cells across the diameter, while axisymmetric ($n = 0$) solutions correspond to an even number of rolls across the diameter. Alternation between these two modes as the critical mode when the aspect ratio of the cylinder is increased allows the flow structure to adjust to the changing geometry with the least amount of distortion to the width-to-depth ratio of an individual recirculation. This alternation of the favoured azimuthal symmetry as the aspect ratio of the cylinder is increased causes the crossings of the modal stability curves.

4.4.2. General results for binary fluid mixtures. The focus will now be changed to how the composition of a binary system affects the critical Rayleigh number. Figures 15 and 16 show the

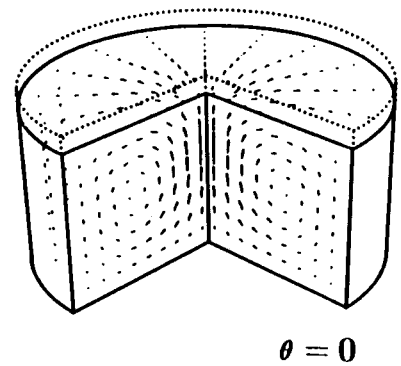

Figure 13. 3D perspective of 1 axisymmetric radial roll in a cylinder with $\gamma = 1$

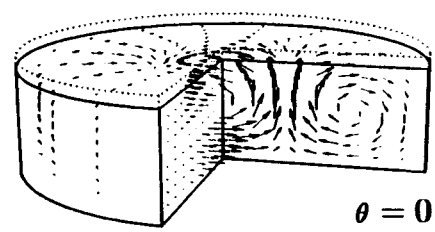

Figure 14. 3D perspective of 1·5 antisymmetric radial rolls in a cylinder with $\gamma = 1{\cdot}8$

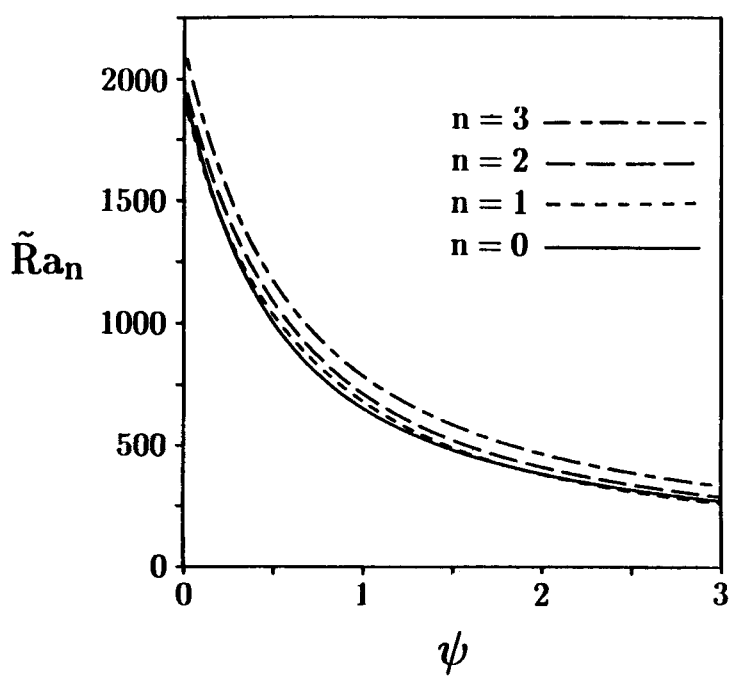

Figure 15. Modal stability curves as a function of ψ for $\psi \leq 3$ with a conducting sidewall

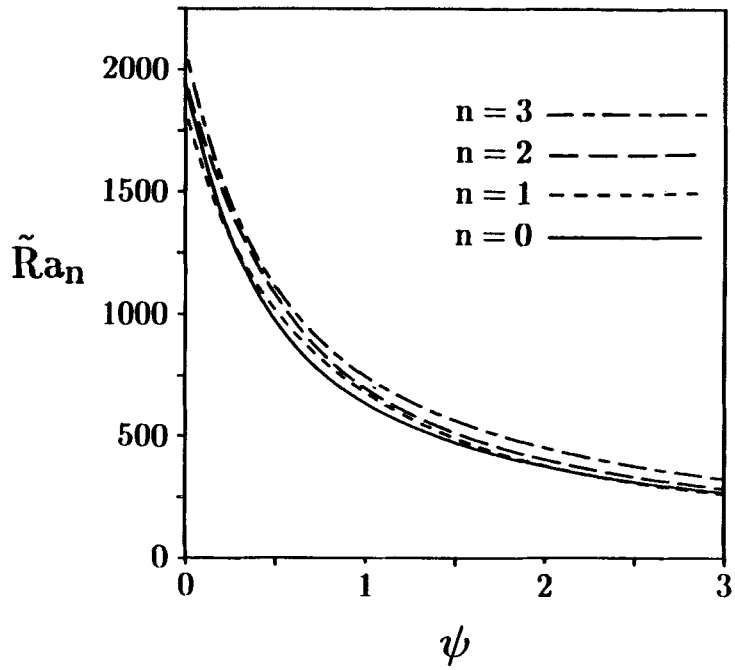

Figure 16. Modal stability curves as a function of ψ for $\psi \leq 3$ with an insulating sidewall

modal stability limits as a function of the Soret parameter ψ for a cylinder with $\gamma = 1{\cdot}8$ and a conducting or insulating sidewall respectively. (Note that these curves were computed with $\zeta = 0$.) $\tilde{Ra}_n$ decreases rapidly for each mode as ψ increases. In comparing the effect of ψ on $\tilde{Ra}_n$ with the effect of γ, the reader should be aware that the scale of the ordinate is greatly expanded in these figures compared to the scale in Figures 9–12, and consequently the modal stability curves appear compressed and their fluctuations less dramatic. Nonetheless, the stability curves for the $n = 0$ and $n = 1$ modes as a function of ψ clearly cross, as they do as a function of aspect ratio. Recall that $n = 1$ is the critical mode for a monocomponent fluid at this aspect ratio, which corresponds here to $\psi = 0$. Then the $n = 1$ mode remains the critical mode for small ψ, up to about $\psi = 0{\cdot}21$ for a cylinder with a conducting sidewall or about $\psi = 0{\cdot}26$ for a cylinder with an insulating sidewall. From these limits up to about $\psi = 1{\cdot}85$ for a cylinder with a conducting sidewall or about $\psi = 2{\cdot}16$ for a cylinder with an insulating sidewall, $n = 0$ is the critical mode. For values of ψ greater than these last two limits, the $n = 1$ mole is always the critical mode regardless of how large ψ is.

The crossings of the modal stability curves in Figures 15 and 16 are again controlled by the roll structure, but here the roll structure for each mode is modulated by ψ rather than γ. As ψ is increased, concentration effects become more important, and the rate at which a fluid parcel can equilibrate in density is decreased. This leads to rolls with greater width-to-depth ratios for greater ψ, which affects the modal stability structure. A detailed explanation of the physics affecting the aspect ratio of an individual recirculation as a function of ψ will be presented in Part II.

To illustrate the impact the Soret effect can have on the stability of systems in which it plays a very strong role, Figure 17 displays $\tilde{Ra}_0$ as a function of ψ over several orders of magnitude of ψ for several different aspect ratios. Figure 18 shows the comparable results for $\tilde{Ra}_1$ as a function

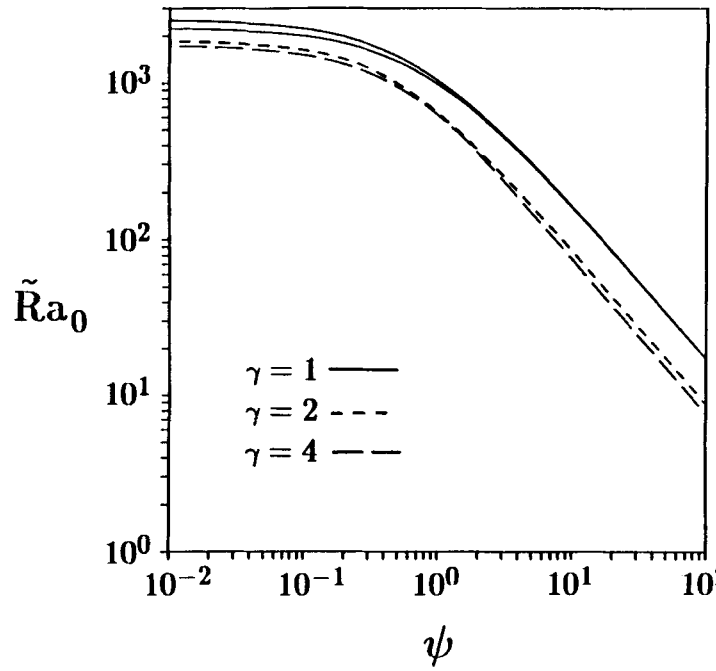

Figure 17. Stability curves for $n = 0$ for $10^{-2} \leq \psi \leq 10^2$

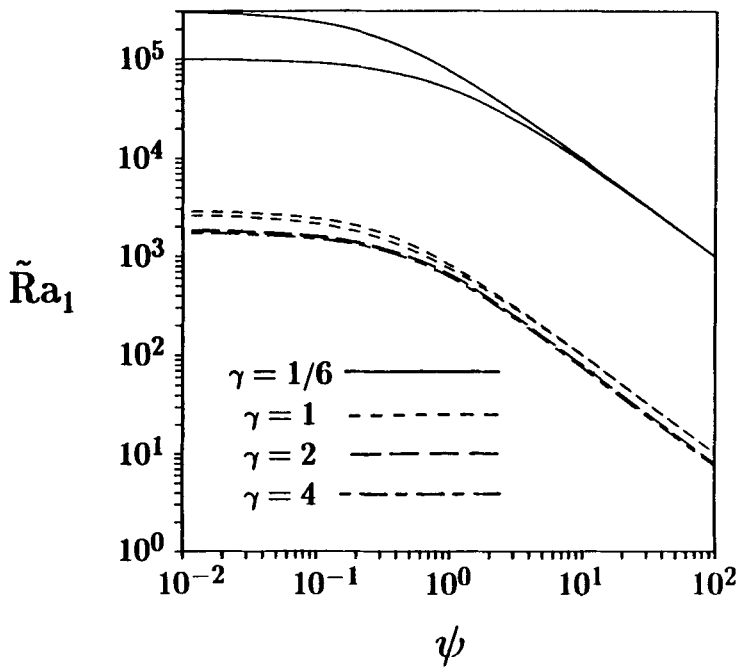

Figure 18. Stability curves for $n = 1$ for $10^{-2} \leq \psi \leq 10^2$

of ψ. The modal stability limits for both sets of boundary conditions (i.e. a cylinder with a conducting sidewall and also one with an insulating sidewall) are plotted together on each figure, using the same line-style for both cases for a given aspect ratio. For the cases shown, these correspond to the upper and lower limits of $\tilde{Ra}_n$ for all wall conductivities at each value of γ plotted for $\zeta = 0$ (i.e. neglecting the Dufour effect). The lower-magnitude Rayleigh numbers always occur for the insulating sidewall case. Note that much of the *structure* of the modal stability curves is lost on the log scale, but the *magnitude* of the Soret contibution is illustrated. All of the remaining figures will be similar in that they will show stability limits for both sets of boundary conditions plotted together. The Soret effect plays a major role in lowering the stability of systems with large ψ, lowering $\tilde{Ra}_n$ by orders of magnitude. Values of ψ of order 10 or even 100 are not unusual. In the limit of large ψ it is found that with $\zeta = 0$, $\tilde{Ra}_n \to f(\gamma)/\psi$ as $\psi \to \infty$.[31] The function $f(\gamma)$ varies relatively slowly with γ; for example, $f(1{\cdot}8) \approx 810$, compared to the result found by Gutkowicz-Krusin *et al.*[27] for a horizontally infinite fluid layer, namely $f(\gamma) \to 720$ for $\gamma \to \infty$.

In order to give a more complete sense of the stability limits of binary mixtures as a function of ψ, Figure 19 displays $\tilde{Ra}_0$ as a function of ψ over the range $-1{\cdot}5 \leq \psi \leq 1{\cdot}5$ for both the conducting and insulating sidewall cases, and Figure 20 shows the analogous results for $\tilde{Ra}_1$. The most interesting feature of these figures is the appearance of a second, negative Rayleigh number branch. This branch will be discussed shortly, but first we consider the more intuitive, positive Rayleigh number branch. For negative ψ we again see that the Soret effect plays a major role in determining the stationary stability limit, although here it tends to increase $\tilde{Ra}_n$ by driving the denser species preferentially towards the warmer, bottom boundary. Recall that as $\psi \to -\infty$, $S \to -1$ from above. Thus as ψ gets increasingly negative for $\alpha > 0$, the increasing contribution

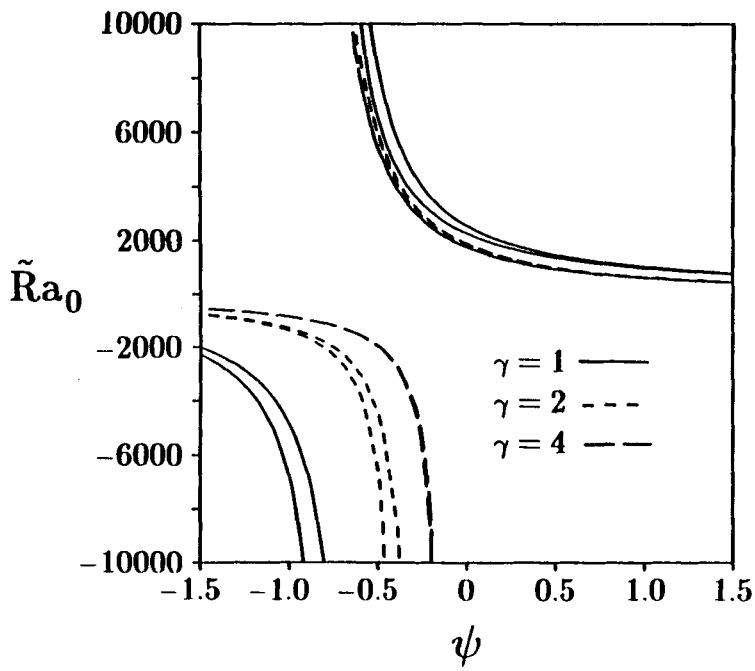

Figure 19. Stability curves for $n = 0$ for $-1{\cdot}5 \leq \psi \leq 1{\cdot}5$ showing both branches

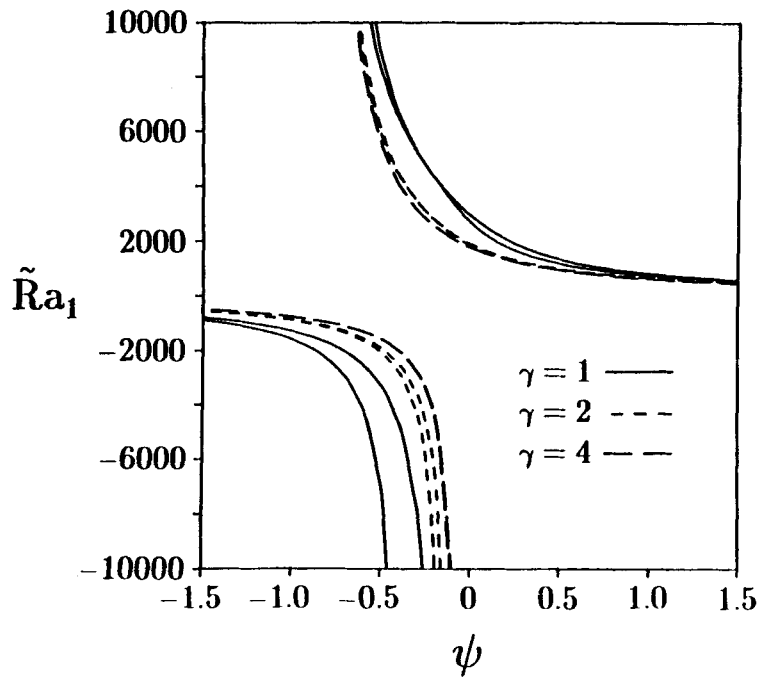

Figure 20. Stability curves for $n = 1$ for $-1{\cdot}5 \leq \psi \leq 1{\cdot}5$ showing both branches

from the Soret effect tends to destroy the density gradient resulting from the thermal contribution. Accordingly, Figures 19 and 20 suggest that $\tilde{Ra}^c \to \infty$ as $\psi \to -\infty$ for heating from below. There is no physical reason why $\tilde{Ra}^c$ should tend to infinity as $\psi \to -1$, as found by Gutkowicz-Krusin *et al.*,[27] or as $S \to -0{\cdot}01$, as found by Schechter *et al.*[13] No such behaviour was found here. However, for $\psi < 0$ (and $\alpha > 0$) with heating from below, unless the magnitude of ψ is small, the onset of convection usually occurs as an oscillatory instability which is driven by the opposing contributions to the density field from the temperature and concentration fields and the differing relaxation times for these two contributions.

A fascinating but unintuitive result is that fluid systems with $\psi < 0$ become unstable to stationary disturbances when heated from *above*, because when $\psi < 0$ the Soret effect tends to drive the denser component towards the warmer region of the container for $\alpha > 0$. (For $\alpha < 0$ the fluid will again have an adverse density profile, which will tend to cause instability in the obvious way.) Thus for $\psi < 0$ (with $\alpha > 0$) there is a second solution branch which is characterized here by negative values of the Rayleigh number, since ΔT for this case is of the opposite sign to that used in the definition of the Rayleigh number. This unexpected phenomenon of systems that are unstable when heated from above has resulted in the determination of erroneous Soret parameters for certain liquid systems. Noting that $\psi < 0$ corresponds to $-1 < S < 0$, so that the thermal contribution to the density gradient is dominant, the negative Rayleigh number branch $\alpha > 0$ and heating from above corresponds to a stationary instability in which the density gradient is *negative*, so that the density decreases from bottom to top. This possibility was first analyzed by Schechter *et al.*[13] for a laterally unbounded system. The mchanism for the instability in this case relies on the difference in relaxation times between perturbations in temperature and concentration. The ratio of the time scale for conduction to that for ordinary diffusion is inversely proportional to κ/D. For liquids, typically $\kappa/D \gg 1$, so that the relaxation time for a perturbation

in temperature is much shorter than for a perturbation in concentration. For $\psi < 0$ (and $\alpha > 0$) the denser species tends to migrate preferentially towards the top when heating is from above. Consequently, the Soret effect partially mitigates the thermal contribution to the density gradient, although the density gradient remains negative. If a parcel of fluid is displaced upwards, it will be denser than its surroundings because of its lower temperature, but it will also be leaner in the more dense species. If $\kappa/D \gg 1$ it will equilibrate faster in temperature than in concentration. Consequently, upon reaching a state near thermal equilibrium, it will be more buoyant than its surroundings because of its lower concentration of the denser species, and will tend to continue to rise. The opposite tendency will exist for a parcel of fluid displaced downwards. If the rate of conversion of the potential energy of a displaced parcel into kinetic energy is faster than the dissipation of its potential energy by diffusion and conduction and its kinetic energy by viscous forces, a flow will ensue. In contrast, for gas mixtures it is unlikely that ψ will be less than zero. Thus even if the Soret and Dufour effects act to increase the separation of the relaxation times for perturbations in temperature and concentration, it is unlikely that gaseous mixtures could become unstable when heated from above, which seems somewhat contrary to the suggestion of Gutkowicz-Krusin *et al.*[27] Figures 21 and 22 complete the stationary stability picture by showing the negative Rayleigh number branches over a range of negative ψ. Figure 21 displays $\tilde{Ra}_0$ for both sidewall boundary conditions, while Figure 22 gives the analogous limits for Ra_1.

5. CONCLUSIONS

It is clear from the previous figures displaying various marginal stationary stability limits that the stabilizing influence of viscous forces at the sidewall diminishes rapidly as γ increases for

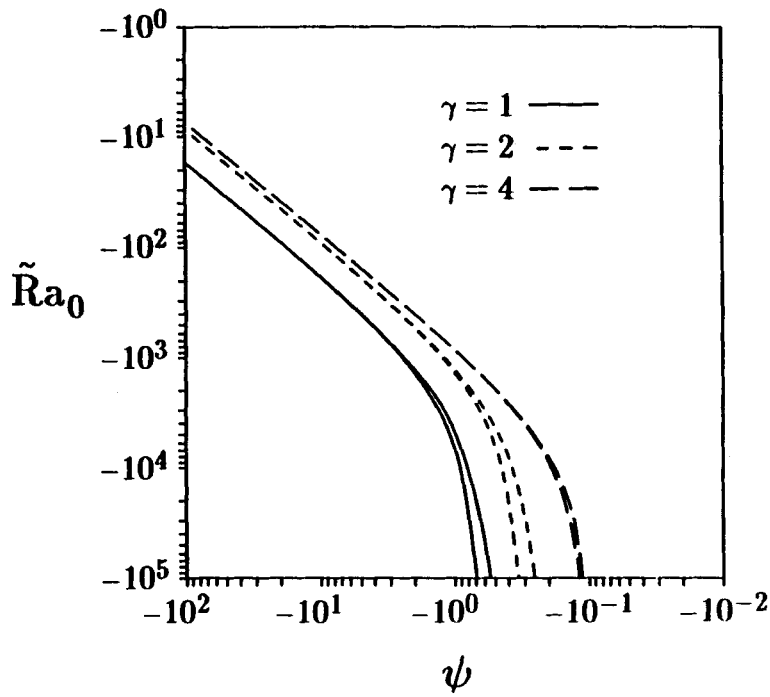

Figure 21. Stability curves for $n = 0$ for $-10^2 \leq \psi \leq -10^{-2}$ with heating from above

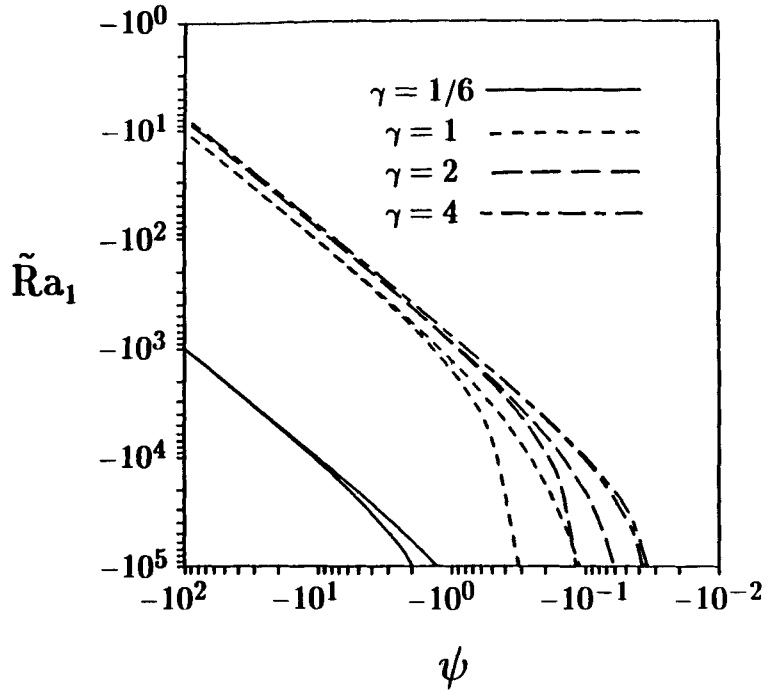

Figure 22. Stability curves for $n = 1$ for $-10^2 \leq \psi \leq -10^{-2}$ with heating from above

approximately $\gamma < 2$. As γ increases beyond about $\gamma = 2$, the stability limit curves for all of the modes asymptotically approach the critical Rayleigh number for a horizontally infinite fluid layer, as previously discussed. This reflects the rapidly diminishing fraction of the total boundary area contributed by the sidewall as γ increases towards approximately $\gamma = 2$, and the relatively slower change after that. The ratio of the area contributed to the boundary by the top and bottom of the container together compared to that contributed by the sidewall is precisely γ, while the *fraction* of the boundary area contributed by the sidewall is $1/(1+\gamma)$. Thus while at $\gamma = 1$ the sidewall represents half of the boundary, at $\gamma = 2$ the ends donate twice the area of the sidewall, so that the fraction of the boundary contributed by the sidewall is only about 33%. A further doubling of the aspect ratio from $\gamma = 2$ to $\gamma = 4$ represents a decrease in the fraction of the boundary contributed by the sidewall of only about 13%, from approximately 33% to 20%, which is a much smaller change in the fraction of the boundary donated by the sidewall for a twofold change in γ. Thus for aspect ratios less than about $\gamma = 2$ the viscous forces at the sidewall stabilize the system substantially relative to a horizontally infinite fluid layer, while for larger γ the viscous inhibition of convection via the sidewall is much smaller. Nonetheless, even for larger aspect ratios the presence of the sidewall greatly influences the spatial configuration of the flow, temperature and concentration fields. At the onset of convection for a given fluid mixture, the azimuthal symmetry of the flow is completely determined by the aspect ratio of the cylinder for the range of aspect ratios that have been considered in this work, except at the values of γ at which two modes are critical, i.e. at the crossings of the modal stability curves. (The spatial configurations of flows for these double-point values of γ near the onset of convection can only be ascertained by non-linear analysis, which will be the subject of a subsequent paper.) Comparing

the results described herein with the results of Rosenblat,[48] who solved the monocomponent problem allowing the flow solution to violate the no-slip condition at the sidewall, it is clear that the no-slip condition must be satisfied in order to predict the correct azimuthal symmetry at the onset of convection.

Finally, the Soret effect has been found to have a potentially major influence on the stability of binary fluid systems and can also greatly affect the flow configuration at the onset of convection. At larger values of ψ the increased Soret effect contribution drives the system towards fewer and consequently longer rolls. Ultimately, for a mixture with a sufficiently large value of ψ, convection sets in as one antisymmetric roll which completely fills the cylinder. The results which have been presented suggest a multitude of interesting and important phenomena which would be worthy subjects for experimental study.

ACKNOWLEDGEMENTS

The authors wish to acknowledge the Scientific Affairs Division of NATO for providing support for this research. In addition, R.L.S. and G.R.H. would like to acknowledge support provided by NASA through the Center for Low-Gravity Fluid Mechanics and Transport Phenomena at the University of Colorado. Also G.R.H. and R.L.S. would like to acknowledge the John von Neumann National Computer Center for providing computer resources. We also would like to acknowledge one of the reviewers for making some very constructive comments.

APPENDIX: NOMENCLATURE

A_{jkn} or A_{jk}	coefficients in the velocity field representation
$a_{rsjk}, \ldots y_{rjsk}$	coefficients resulting from evaluation of Galerkin integrals
B_{jkn} or B_{jk}	coefficients in the temperature field representation
C_{jkn} or C_{jk}	coefficients in the η-field representation
C_p	specific heat at constant pressure
D	mass diffusivity
D_{jkn} or D_{jk}	coefficients in non-axisymmetric velocity field representation
D'	Soret coefficient
D''	Dufour coefficient
E_{jkn}	coefficients in the pressure field representation
$\mathbf{e}_r$, $\mathbf{e}_\theta$, $\mathbf{e}_z$	cylindrical unit vectors
F_D	Dufour parameter
$\mathbf{f}$ and $\tilde{\mathbf{f}}$	arbitrary function and complex conjugate (Section 3.2 only)
$\mathbf{g}$	arbitrary function (Section 3.2. only)
g	magnitude of gravitational acceleration
$\mathbf{g}$	gravitational acceleration
I_n	nth-order Bessel function of the second kind
i	$\sqrt{(-1)}$
J_n	nth-order Bessel function of the first kind
$\mathbf{j}_1$	mass flux of species 1
k	thermal conductivity
k_T^{mass}	mass thermal diffusion ratio
L	height of cylinder
n	azimuthal wave number (mode number)
$\mathbf{n}$	unit normal vector

$\mathbf{O}_{jkn}$	axisymmetric velocity basis function
p	pressure
P	spatial dependence of p in the linear stability problem
$\tilde{Pr}$	modified Prandtl number
$\mathbf{q}$	heat flux
R	radius of cylinder
Ra	Rayleigh number (for a monocomponent fluid)
$\tilde{Ra}$	modified Rayleigh number (for a binary fluid)
$\mathscr{R}$ and $\tilde{\mathscr{R}}$	Rayleigh numbers based on the cylinder radius
$\hat{\mathscr{R}}$	normalized value of $\tilde{\mathscr{R}}$
r	radial co-ordinate
S	Soret separation number
s	generic scalar
$\tilde{Sc}$	modified Schmidt number
T	temprature
T_B	temperature of cylinder bottom
T_T	temperature of cylinder top
ΔT	$\equiv T_B - T_T$
$\bar{T}$	volume-averaged temperture
t	time
$\mathbf{u}$	velocity
$\mathbf{U}$	spatial dependence of $\mathbf{u}$ in the linear stability problem
V	volume of cylinder
$\mathbf{v}$	generic vector
$\mathbf{V}_{jkn}$	non-axisymmetric velocity basis function
W_1	mass fraction of species 1
$\bar{W}_1$	volume-averaged weight fraction of species 1
$\mathbf{W}_{jkn}$	non-axisymmetric velocity basis function
X_j	z basis function for the velocity field
X_{Xe}	mole fraction of xenon
Y_k	radial velocity basis function
z	vertical co-ordinate

Greek symbols

α	thermal expansion coefficient
$\tilde{\alpha}$	modified thermal expansion coefficient (binary fluid)
α_1	modified thermal diffusivity (binary fluid)
α_2	$\equiv \alpha_1 \gamma_2 / D$
β	solutal expansion coefficient
β_2	modified mass diffusivity (binary fluid)
γ	cylinder aspect ratio ($\gamma \equiv R/L$)
γ_1	Dufour coefficient
γ_2	Soret coefficient
ζ	dimensionless Dufour parameter
η	transformed concentration variable
Θ	spatial dependence of T in linear stability problem
θ	azimuthal co-ordinate

κ	thermal diffusivity
Λ_{jkn}	η basis function
$\mu_1^{W_1}$	partial derivative of the chemical potential of species 1 with respect to W_1, its mass fraction
ν	kinematic viscosity
Π_{jkn}	pressure basis function
ρ	mass density
σ	complex amplification factor ($\sigma = \sigma_r + i\sigma_i$)
Φ_{jkn}	temperature basis function
ψ	dimensionless Soret parameter

Superscripts

c	critical Rayleigh number
d	dimensional quantity
T	transpose of a matrix
$'$	differentiation with respect to the independent variable, r or z

Subscripts

1	property of component one
2	property of component two
B	evaluated at bottom of cylinder
i	imaginary part
n	corresponds to mode n
r	real part
T	evaluated at top of cylinder

Special symbol

∂V	boundary of cylinder

REFERENCES

1. H. E. Huppert and J. S. Turner, 'Double-diffusive convection', *J. Fluid Mech.*, **106,** 299–329 (1981).
2. G. Veronis, 'On finite amplitude instability in thermohaline convection', *J. Marine Res.*, **23,** 1–17 (1965).
3. R. L. Sani, 'On finite amplitude roll cell disturbances in a fluid layer subjected to heat and mass transfer', *AIChE J.*, **11,** 971–980 (1965).
4. S. R. de Groot and P. Mazur, *Nonequilibrium Thermodynamics*, North-Holland, Amsterdam, 1962, Chap. 11.
5. J. N. Agar and J. C. R. Turner, 'Thermal diffusion in solutions of electrolytes', *Proc. R. Soc. Lond. A*, **255,** 307–330 (1960).
6. J. C. Legros, W. A. Van Hook and G. Thomaes, 'Convection and thermal diffusion in a solution heated from below', *Chem. Phys. Lett.*, **1,** 696–698 (1968).
7. J. C. Legros, W. A. Van Hook and G. Thomaes, 'Convection and thermal diffusion in a solution heated from below II. The system $CHBr_2 \cdot CHBr_2$–$CHCl_2 \cdot CHCl_2$', *Chem. Phys. Lett.*, **2,** 249–250, (1968).
8. D. T. J. Hurle and E. Jakeman, 'Soret-driven thermosolutal convection', *J. Fluid Mech.*, **47,** 667–687 (1971).
9. D. T. J. Hurle and E. Jakeman, 'Natural oscillations in heated fluid layers', *Phys. Lett.*, **43A,** 127–129 (1973).
10. D. T. J. Hurle and E. Jakeman, 'Thermal oscillations in convecting fluids', *Phys. Fluids*, **16,** 2056–2059 (1973).
11. J. K. Platten and G. Chavepeyer, 'Soret driven instability', *Phys. Fluids*, **15,** 1555–1557 (1972).
12. J. K. Platten and G. Chavepeyer, 'Oscillatory motion in Bénard cell due to the Soret effect', *J. Fluid Mech.*, **60,** 305–319 (1973).
13. R. S. Schechter, I. Prigogine and J. R. Hamm, 'Thermal diffusion and convective stability', *Phys. Fluids*, **15,** 379–386 (1972).

14. D. T. J. Hurle and E. Jakeman, 'Significance of the Soret effect in the Rayleigh–Jeffreys' problem', *Phys. Fluids*, **12**, 2704–2705 (1969).
15. J. K. Platten and G. Chavepeyer, 'Oscillations in a water–ethanol liquid heated from below', *Phys. Lett.*, **40A**, 287–288 (1972).
16. J. C. Legros, J. K. Platten and P. G. Poty, 'Stability of a two-component fluid layer heated from below', *Phys. Fluids*, **15**, 1383–1390 (1972).
17. T. G. L. Shirtcliffe, 'An experimental investigation of thermosolutal convection at marginal stability', *J. Fluid Mech.*, **35**, 677–688 (1969).
18. F. Rosenberger, 'Crystallization from the vapor', in *Materials Science Experiments in Space, Contractor Report 2842*, NASA Scientific and Technical Information Office, 1978, pp. 39–43.
19. B. R. Sundheim and J. D. Kellner, 'Thermoelectric properties of the molten silver nitrate–sodium nitrate system', *J. Phys. Chem.*, **69**, 1204–1208 (1965).
20. J. Bataille, J. Dupuy, Ph. Girodroux and H. Mellon, 'On the possibility of measuring the Soret coefficient under zero gravity conditions: a preliminary stability analysis', *Space Res.*, **18**, 507–509 (1977).
21. J. L. Castillo and M. G. Velarde, 'Microgravity and the thermoconvective stability of a binary liquid layer open to the ambient air', *J. Non-Equilib. Thermodyn.*, **5**, 111–124 (1980).
22. D. Villers and J. K. Platten, 'Heating curves in the two-component Bénard problem', *J. Nonequilib. Thermodyn.*, **9**, 131–146 (1984).
23. R. S. Schechter, M. G. Velarde and J. K. Platten, 'The two-component Bénard problem', *Adv. Chem. Phys.*, **26**, 265–301 (1974).
24. J. K. Platten and G. Chavepeyer, 'Finite amplitude instability in the two component Bénard problem', *Adv. Chem. Phys.*, **32**, 281–322 (1975).
25. P. L. G. Ybarra and M. G. Velarde, 'The role of Soret and Dufour effect on the stability of a binary gas layer heated from below or above', *Geophys. Astrophys. Dyn.*, **13**, 83–94 (1979).
26. D. Gutkowicz-Krusin, M. A. Collins and J. Ross, 'Rayleigh–Bénard instability in nonreactive binary fluids. I. Theory', *Phys. Fluids*, **22**, 1443–1460 (1979).
27. D. Gutkowicz-Krusin, M. A. Collins and J. Ross, 'Rayleigh–Bénard instability in nonreactive binary fluids. II. Results', *Phys. Fluids*, **22**, 1451–1460 (1979).
28. J. R. Abernathey and F. Rosenberger, 'Soret diffusion and convective stability in a closed vertical cylinder', *Phys. Fluids*, **24**, 377–381 (1981).
29. E. Crespo and M. G. Velarde, 'Two-component Bénard convection in cylinders', *Int. J. Heat Mass Transfer*, **25**, 1451–1456 (1982).
30. M. G. Velarde, E. Crespo and P. L. Garcia-Ybarra, 'Corrigenda et addenda to two-component Bénard convection in cylinders', *Int. J. Heat Mass Transfer*, **28**, 311–313 (1985).
31. D. Henry, 'Instabilities oscillatoires et monotones dans le cas d'un mélange binaire, avec effet Soret, dans un cylindre vertical soumis a un gradient de temperature axial', *Thèse de Docteur Ingénieur*, L'Université Claude Bernard, Lyon 1, 1983.
32. D. Henry and B. Roux, 'Stationary and oscillatory instabilities for mixture subjected to Soret effect in vertical cylinder with axial temperature gradient', in *Proc. 4th European Symp. on Material Sciences Under Microgravity (ESA SP-191)*, Madrid, 5–8 April 1983, ESA, Paris, 1983, pp. 142–152.
33. G. R. Hardin, 'Soret and Dufour effects in buoyancy-driven instability of a bounded, cylindrical, binary fluid layer', *Master's Thesis*, University of Colorado, Boulder, 1983.
34. W. T. Mitchell and J. A. Quinn, 'Thermal convection in a completely confined fluid layer', *AIChE J.*, **12**, 1116–1124 (1966).
35. K. Stork and U. Müller, 'Convection in boxes: an experimental investigation in vertical cylinders and annuli', *J. Fluid Mech.*, **71**, 231–240 (1975).
36. L. Onsager, 'Reciprocal relations in irreversible processes, I', *Phys. Rev.*, **37**, 405–426 (1931).
37. L. Onsager, 'Reciprocal relations in irreversible processes, II', *Phys. Rev.*, **38**, 2265–2279 (1931).
38. E. A. Spiegel and G. Veronis, 'On the Boussinesq approximation for a compressible fluid', *Astrophys. J.*, **131**, 442–447 (1960).
39. R. W. Zeren, 'Thermal instability in horizontal two-fluid layers', *Ph.D. Thesis*, Standford University, March 1970 (Report *FM5*, Thermal Sciences Division, Department of Mechanical Engineering).
40. L. V. Nikitin and E. I. Ryzhak, 'Accuracy of the Boussinesq approximation for a incompressible fluid', *Fluid Dyn.* **16**, 174–180 (1981).
41. G. S. Charlson and R. L. Sani, 'Thermoconvective instability in a bounded cylindrical fluid layer', *Int. J. Heat Mass Transfer*, **13**, 1479–1496 (1970).
42. B. A. Finlayson, *The Method of Weighted Residuals and Variational Principles, With Applications in Fluid Mechanics, Heat and Mass Transfer*, Academic Press, New York, 1972.
43. G. S. Charlson and R. L. Sani, 'On thermoconvective instability in a bounded cylindrical fluid layer', *Int. J. Heat Mass Transfer*, **14**, 2157–2160 (1971).
44. J. C. Buell and I. Catton, 'The effect of wall conduction on the stability of a fluid in a right circular cylinder heated from below', *J. Heat Transfer*, **105**, 255–260 (1983).
45. E. Crespo, P. Bontoux, C. Smutek, B. Roux, G. Hardin, R. Sani and F. Rosenberger, 'Three-dimensional simulations of convection regimes in cylindrical ampoules. Comparisons with theoretical analyses and experiments', in *Proc. 6th*

European Symp. on Material Sciences Under Microgravity Conditions (*ESA SP-256*), Bordeaux, 2–5 December 1986, ESA, Paris, 1987, pp. 529–537.
46. R. L. Sani, 'Convective instability', *Ph.D. Thesis*, University of Minnesota, Minneapolis, 1963.
47. J. M. Olson and F. Rosenberger, 'Convective instabilities in a closed vertical cylinder heated from below. Part 1. Monocomponent gases', *J. Fluid Mech.*, **92,** 609–629 (1979).
48. S. Rosenblat, 'Thermal convection in a vertical circular cylinder', *J. Fluid Mech.*, **122,** 395–410 (1982).